

AD-A121 734

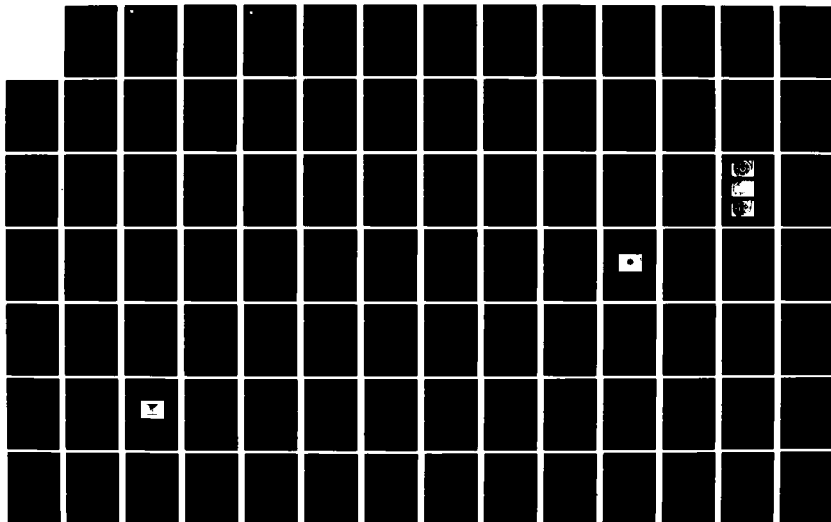
SYSTEM TO MEASURE CARRIER DRIFT VELOCITY IN  
SEMICONDUCTOR MATERIALS(U) WASHINGTON UNIV ST LOUIS MO  
DEPT OF ELECTRICAL ENGINEERING G M HOMSEY ET AL  
AUG 82 82-4-ONR N00014-79-C-0840

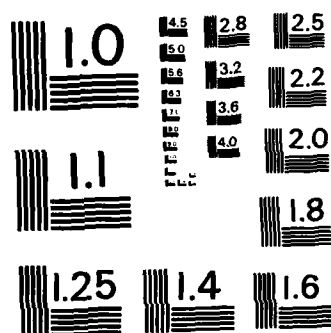
1/2

UNCLASSIFIED

F/G 20/12

NL





MICROCOPY RESOLUTION TEST CHART  
NATIONAL BUREAU OF STANDARDS-1963-A



(12)

AD A121734

# SYSTEM TO MEASURE CARRIER DRIFT VELOCITY IN SEMICONDUCTOR MATERIALS

G.M. HOMSEY  
F.J. ROSENBAUM  
R.E. GOLDWASSER

Department of Electrical Engineering  
Washington University  
St. Louis, MO 63130

AUGUST 1982

DTIC  
ELECTE  
NOV 22 1982  
A

Technical Report ONR-82-4

Office of Naval Research  
Arlington, VA 22217

Reproduction, in whole or in part, is permitted for any purpose of the U.S. Government.

Contract: N00014-79-C-840  
Contract Authority: NR SRO-004

Approved for public release; distribution unlimited.

82 11 22 102

DTIC FILE COPY





WASHINGTON  
UNIVERSITY  
IN ST. LOUIS

## **SYSTEM TO MEASURE CARRIER DRIFT VELOCITY IN SEMICONDUCTOR MATERIALS**

G.M. HOMSEY  
F.J. ROSENBAUM  
R.E. GOLDWASSER

Department of Electrical Engineering  
Washington University  
St. Louis, MO 63130

**AUGUST 1982**

Technical Report NR-82-4

Office of Naval Research  
Arlington, VA 22217

Reproduction, in whole or in part, is permitted for any purpose of the U.S. Government.

Contract: N00014-79-C-840  
Contract Authority: NR SRO-004

Approved for public release; distribution unlimited.

TABLE OF CONTENTS

No.		Page
1.	Introduction .....	1
	1.1 Previous Measurement Approaches .....	9
	1.2 Scope of this Work .....	12
2.	Theoretical Basis for $v(E)$ Measurements .....	15
	2.1 The Carrier Velocity - Current Phase Relationship .....	15
	2.2 Nonuniform Electric Field Solution .....	19
3.	System Realization .....	28
	3.1 Electron Gun and Power Supply .....	28
	3.2 6 GHz Modulator .....	35
	3.3 Sample and Sample Holder Assembly .....	40
	3.4 DC Characterization of the Apparatus .....	47
	3.5 Tuning and Amplification of the Detected Sample Signal .....	55
	3.5.1 Double Stub Tuner .....	55
	3.5.2 Cascaded Amplifiers .....	56
	3.5 Measurement Scheme .....	56
4.	Results .....	59
	4.1 Measured Results .....	59
	4.2 Analysis of Windhorn's Data .....	68
	4.3 Comparison of Our Results with Windhorn's Results .....	73
5.	Conclusions .....	76
	5.1 Limitations of the Uniform Field Approximation .....	76
	5.2 Summary .....	78
	5.3 Recommendations .....	80

**TABLE OF CONTENTS**  
**(continued)**

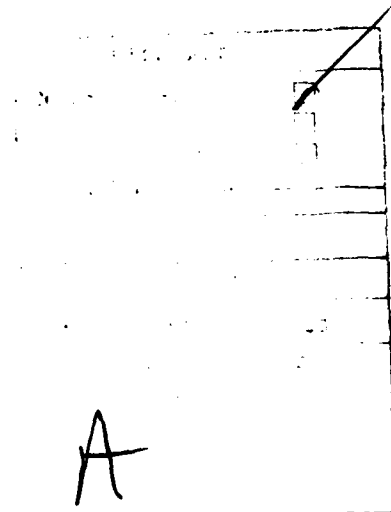
No.	Page
6. Acknowledgements .....	82
7. Appendices .....	83
Appendix 7.1 Computer Programs .....	84
Appendix 7.2 Machine Drawings .....	94
Appendix 7.3 Power Supply Circuits .....	100
Appendix 7.4 Sample Lumped Circuit Solution .....	106
8. Bibliography .....	108

LIST OF TABLES

No.	Page
4.1 Measured and adjusted phase vs. applied voltage for the 2A26 #2 sample .....	65
4.2 Adjusted phase vs. applied voltage from T. Windhorn's measurements .....	71



A





LIST OF FIGURES

No.	Page
1.1 Reported velocity-field characteristic for GaAs (3)	2
1.2 Charge motion in a uniform electric field in a vacuum diode .....	4
1.3 Electric field profile .....	7
1.4 Evans and Robson's time-of-flight apparatus (3) ....	10
1.5 Block diagram of $v(E)$ experimental apparatus .....	13
2.1 Electric field intervals for individual phase measurements .....	22
2.2 Block diagram of the Newton-Raphson iterative method	23
3.1 Electron gun .....	30
3.2 Beam modulation observed on a phosphor target .....	31
3.3 Block diagram of the high voltage supplies .....	32
3.4 Reentrant coaxial cavity modulator body .....	36
3.5 Electric field profile in reentrant coaxial cavity .	37
3.6 6 GHz waveguide launcher .....	39
3.7 GaAs Schottky barrier sample .....	41
3.8 Photograph of a packaged GaAs sample .....	43
3.9 Lumped element representation of the packaged sample with an injected, modulated beam .....	44
3.10 Assembly of sample holder transmission line .....	46
3.11 Sample holder assembly .....	48
3.12 Vacuum envelope assembly .....	49
3.13 Detected current vs. beam potential .....	50
3.14 Current multiplication vs. beam potential .....	52
3.15 Sample current vs. reverse bias .....	53

LIST OF FIGURES  
(continued)

No.	Page
3.16 Beam induced current vs. reverse bias .....	54
3.17 6 GHz $v(E)$ measurement circuit .....	57
4.1 Sample 2A26 capacitance analysis .....	60
4.2 Samples 2A26 and M13 doping profiles .....	61
4.3 Sample 2A26 electric field profile with reverse bias	62
4.4 Sample 2A26 current-voltage relationship .....	63
4.5 Measured $v(E)$ curve for sample 2A26 .....	66
4.6 Low field velocity curve, closeup of Figure 4.5 ....	69
4.7 Electric field profile with reverse bias for T. Windhorn's samples .....	70
4.8 Calculated $v(E)$ curve from Windhorn's phase-voltage data .....	72
4.9 Comparison of calculated $v(E)$ curves .....	74
5.1 Comparison of non-uniform field solution with uniform field solution .....	77
A2.1 6 GHz modulator body .....	95
A2.2 6 GHz waveguide launcher .....	96
A2.3 12 GHz quarter wavelength tuning stub .....	97
A2.4 Sliding stub tuner center conductor .....	98
A2.5 Sliding stub tuner body .....	99
A2.6 Filament supply .....	101
A2.7 High voltage circuit .....	102
A2.8 Regulating circuit H.V. #2 .....	103
A2.9 Regulating circuit H.V. #1 .....	104
A2.10 Switching Circuit .....	105

## SYSTEM TO MEASURE CARRIER DRIFT VELOCITY IN SEMICONDUCTOR MATERIALS

### 1. INTRODUCTION

The electrical behavior of semiconductor devices is strongly dominated by the motion of charge carriers in the electric field present within the device. Particle motion in a crystalline solid differs from that in free space, for example, because the energy transferred from the field to the particle is influenced by the energy band structure of the material, scattering processes which transfer energy from the particle to the crystal lattice and a variety of effects such as trapping, intra- and inter-valley scattering, etc. One means of accounting for these complex effects is to define an average drift velocity for carriers in the presence of an electric field. For some III-V semiconductors, such as GaAs, the velocity-field curve is non-monotonic and exhibits a region of negative differential mobility as shown in Figure 1.1.

The negative differential mobility region on the high field side of the peak gives rise to unique phenomena such as Gunn oscillations (1)\*. Precise knowledge of the drift velocity-electric

\* The numbers in the parentheses in the text indicate reference in the Bibliography.

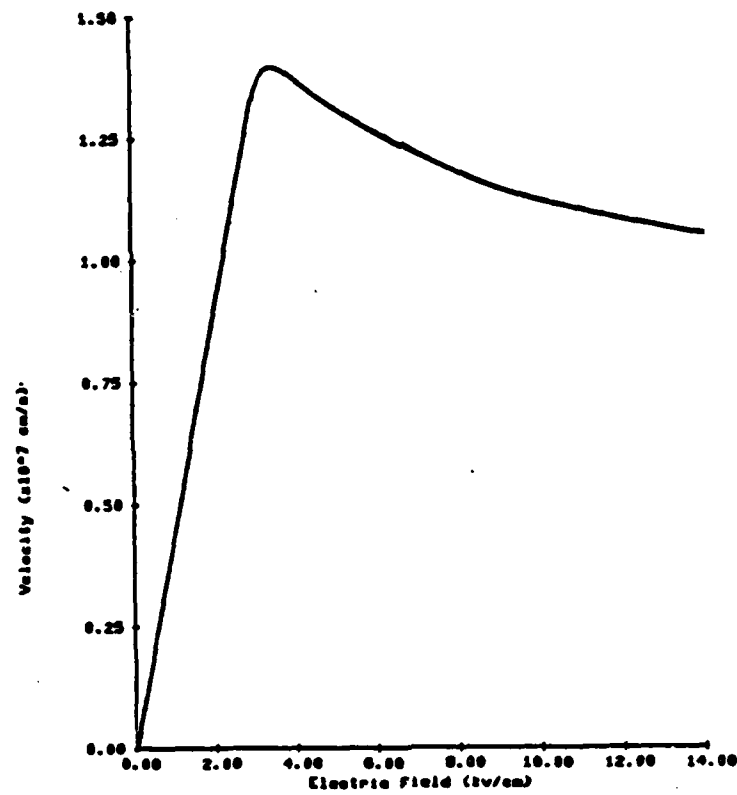


Figure 1.1 Reported velocity-field characteristic for GaAs (3)

field relationship is needed to understand device behavior and to aid in the design and improvement of semiconductor devices such as field effect transistors and Gunn diodes.

The problem of measuring the velocity-field curve can be illustrated by considering the behavior of charge in a vacuum diode. Figure 1.2 shows a parallel plate diode whose plates are separated by a length  $L$  and with a constant internal electric field equal to the applied voltage divided by the length. If a charge layer of electrons,  $\sigma_s$ , is injected between the plates it will induce a surface charge  $\sigma_1$  at  $x=0$  and  $\sigma_2$  on the contact at  $x=L$  where  $\sigma_1$  and  $\sigma_2$  are given by

$$\sigma_1 = -\sigma_s \frac{L-x_1}{L} \quad (1.1)$$

$$\sigma_2 = -\sigma_s \frac{x_1}{L} \quad (1.2)$$

With the applied voltage shown the negative charge sheet,  $\sigma_s$ , will move to the right with some velocity  $v$  and the charge densities at the terminals will change with time, inducing current in the external circuit related to the current density  $J_T$ :

$$J_T = \frac{d\sigma_2}{dt} = -\frac{d}{dt}\left(-\sigma_s \frac{x_1}{L}\right) \quad (1.3)$$

$$J_T = \frac{\sigma_s}{L} \frac{dx_1}{dt} = \frac{\sigma_s}{L} v = \rho v \quad (1.4)$$

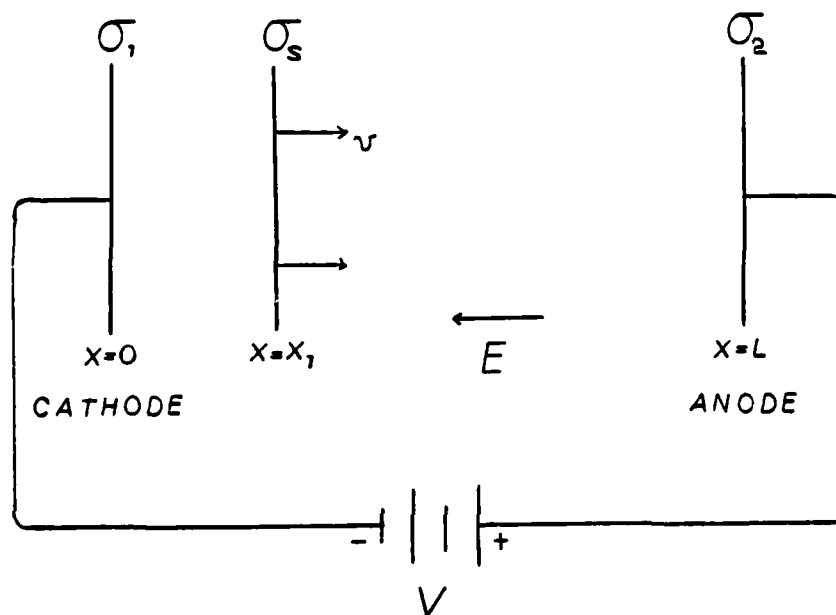


Figure 1.2 Charge motion in a uniform electric field in a vacuum diode.

Here  $\rho$  is the volume charge density and  $v$  is the free space velocity. For most experiments in determining  $v(E)$  this external circuit current is the only observable variable.

In a vacuum diode with a uniform electric field the velocity  $v$  increases with time. However, in a semiconductor the velocity will depend on the  $v(E)$  relation. If a uniform field is present the velocity will be constant. In a typical experiment charge injected into the diode region induces a pulse of current in the external circuit. The pulse rise time is proportional to the rate of charge injection. The pulse width measures the transit time of charge through the diode. The pulse fall time is related to trapping and diffusion of the charge layer during transit.

To measure the velocity within a semiconductor medium, a nonconducting Schottky contact is usually employed. A metal, such as Al, is evaporated on an epitaxial semiconductor layer grown on a conducting substrate that forms the anode. The difference between the metal work function and the n-type semiconductor work function will cause electrons to travel from the material into the metal. This leaves a "depleted" region beneath the metal which has a net positive charge and a negative charge on the metal. An electric field is created with its maximum (negative) value at the metal. It increases to zero within the semiconductor. The electron migration stops when the electrostatic potential of the semiconductor is raised to match the work function differential across the interface. Under increasing reverse bias this depletion region grows into the material.

For a reverse biased Schottky diode the situation is similar to the vacuum diode case except that the cathode is now the Schottky metallization, the anode is the end of the depletion region and the electric field slope is related to the local doping density,  $N_d(x)$ , by Poisson's equation

$$\frac{dE}{dx} = \frac{q}{\epsilon} N_d(x) \quad (1.5)$$

where  $q$  is the electron charge and  $\epsilon$  the dielectric permittivity of the semiconductor medium. The electric field will therefore go from a maximum intensity,  $E_0$ , at the edge of the Schottky contact to zero past the end of the depletion region. Figure 1.3a shows the field profile for an arbitrarily doped Schottky diode of length  $L$  under normal bias. Some epitaxial layers are short enough and sufficiently lightly doped that the electric field extends into the substrate which has a much higher doping concentration. In the substrate the field drops off very quickly with depth making a profile which looks similar to Figure 1.3b. This is called the punched-through case where the electric field has a non-zero value at the end of the epitaxial layer. The contribution of the carrier transit time in the substrate, in this case, is negligible compared to that of the epitaxial layer since the length of field penetration is minute in the heavier doped material. Most velocity-field measurements are done with the sample biased in the punched-through state.



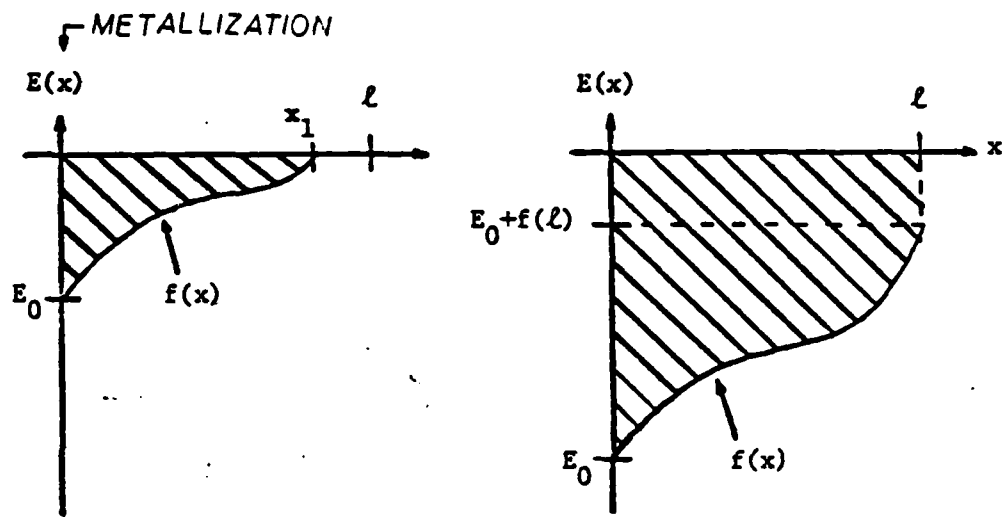


Figure 1.3 Electric field profile (a) not punched through  
(b) punched through

Earlier techniques to determine velocity-field relationships used Schottky diodes with long, lightly doped material. A pulse of electrons was injected at one end with an electron gun and the transit time of the charge across the depletion region was measured. This was known as the time-of-flight technique (2).

Later a modulated sinusoidal signal injection scheme was developed to yield better resolution (3,4,5,6). The phase of the detected signal contains information concerning the transport of charge particles through the lattice. If sufficiently high modulation frequencies are used the semiconductor sample could be small compared to those used for time-of-flight measurements and thus more nearly approximate conditions found in actual devices. These microwave phase (CW) time-of-flight schemes have been used before and show much promise for small samples with high doping levels.

Measuring the time-of-flight mobility of semiconductors is difficult and requires a large amount of equipment. A means of injecting free carriers at a constant rate and known modulation into the active region is needed. Target samples of proper doping profile and epitaxial layer thickness are necessary for detailed analysis of sections of the  $v(E)$  curve. Sensitive signal detection circuitry is required along with an accurate technique of interpreting the measured phase-voltage data and deriving the velocity-field relationship.

Attempts have been made in the past to determine the mobility of certain semiconductors. Some of the previously stated requirements have been considered.

### 1.1 PREVIOUS MEASUREMENT APPROACHES

Electron beam injection methods were employed by J.G. Ruch and G.S. Kino (2) in the time-of-flight measurement scheme. In their experiment the beam was swept across an aperture exposing the target material and the duration of the current pulse in the external circuit divided by the sample length was taken as the velocity. Sample doping was compensated low so a uniform electric field assumption could be made and long samples (300 microns) were used to get measurable pulse widths. These long samples allowed diffusion effects to become significant, enabling diffusion vs. electric field measurements but also increasing the pulse fall time. Uncertainty in the pulse duration along with the lack of system calibration encouraged the investigation of other measurement techniques.

In 1974 Evans and Robson (3) reported data taken using a microwave phase time-of-flight method. Figure 1.4 shows the schematic diagram of their experimental setup. The beam was deflected past the sample face at an RF rate and the phase shift of the external circuit current was measured. The doping concentrations were low and the sample lengths short so a uniform

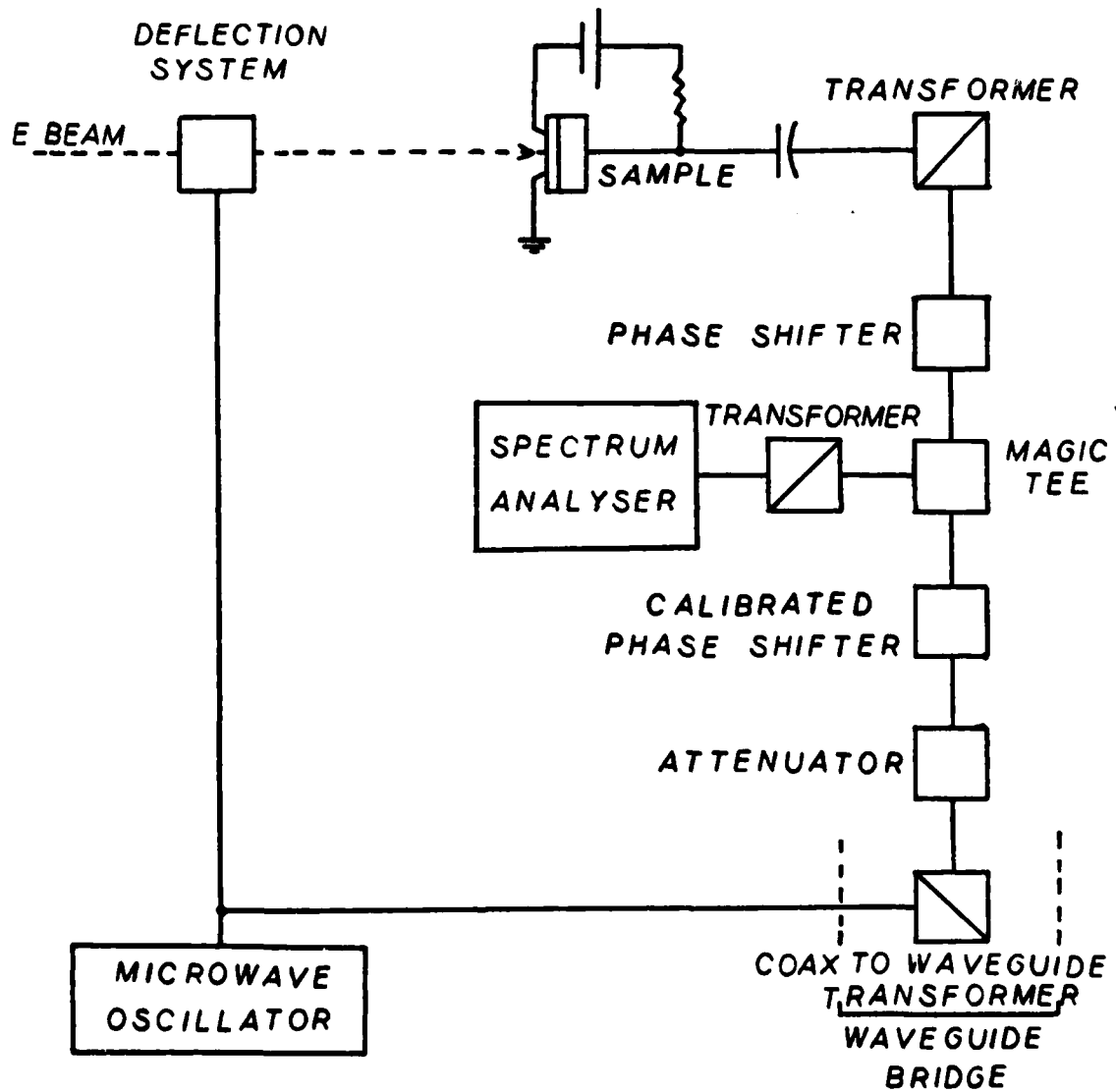


Figure 1.4 Evans and Robson's microwave time-of-flight apparatus (3).

electric field equal to the voltage divided by the epitaxial region length was assumed. Since the electric field was taken to be constant so was the velocity which was calculated from the measured phase using the expression

$$\phi = \frac{\omega l}{2v} \quad (1.6)$$

where  $\omega$  is the microwave radian frequency of the current. This result will be derived later.

The CW method and uniform field approximation are being used at both Cornell University (6) and the University of Illinois (4,5) on Si, GaAs and InGaAs. Besides using low doped samples most of these measurements are being performed at high electric fields where the velocity is more nearly constant to minimize velocity averaging errors.

Monte Carlo simulations (7) using band structure probabilities have predicted the doping and temperature dependence of the  $v(E)$  curve for GaAs and InP. These results can be compared to measured data at high doping levels.

The work here deals with the measurement of the  $v(E)$  curve at low electric fields. It addresses and analyzes the non-uniform field situation, signal detection considerations and numerical methods to relate the measured current-phase to the velocity-field relationship.

## 1.2 SCOPE OF THIS WORK

The system employed in the work reported here is an improved model of the one described in ONR report #80-2 (8) which is similar in design to that of Evans and Robson (3). Figure 1.5 shows a block diagram of the measurement system. An electron beam is modulated at 6 GHz and swept past a Schottky diode face. Carriers are injected through the Schottky contact into the sample with a frequency of 12 GHz since the beam passes the sample aperture twice in one modulation period. The phase of the resulting signal in the external circuit is then measured as a function of applied reverse bias, relative to the reference signal phase, with a Hewlett-Packard automatic network analyzer. Chapter 3 contains a detailed description of the system components and measurement technique. There are a number of advantages this analysis has over the previously mentioned microwave time-of-flight measurements.

The doping profile of the material used in these measurements is well known and so the electric field can be calculated with respect to depth and applied bias. A nonuniform field solution is possible using numerical methods to derive a  $v(E)$  curve which best fits the observed data. This technique also allows the examination of higher doping concentrations than could be done using previous techniques.

This scheme should yield information about the  $v(E)$  curve down to zero electric field. These measurements are then absolute and no

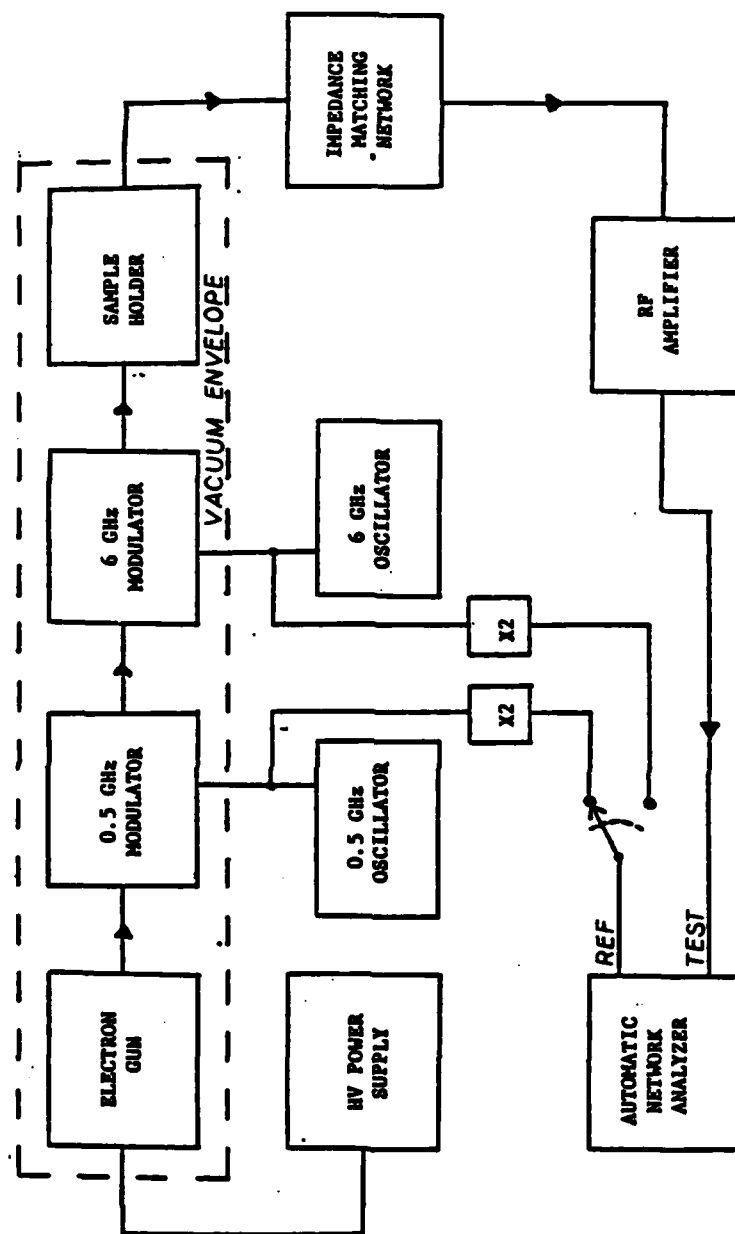


Figure 1.5 Block diagram of  $v(E)$  experimental apparatus.

other data are needed as reference. A Hewlett-Packard ANA under computer control is used to automate the measurements.

The remainder of this report is devoted to describing the theoretical aspects of the measurement, the physical design of the system, and the data generated using this technique. Results are compared to previous experiments and simulations. Conclusions and proposals for improvements are made from these comparisons.



## 2. THEORETICAL BASIS FOR $v(E)$ MEASUREMENTS

Through measurement and interpretation of the external circuit current the carrier velocity-internal electric field relation can be determined. The phase of this current holds enough information to uniquely define the  $v(E)$  curve.

### 2.1 THE CARRIER VELOCITY - CURRENT PHASE RELATIONSHIP

First the current continuity equation within the material must be examined

$$\nabla \cdot \bar{J} = - \frac{\partial \rho}{\partial t} \quad (2.1)$$

This can be simplified if only current density variations in the direction of the applied electric field, say along  $x$ , are considered

$$\frac{\partial J}{\partial x} = - \frac{\partial \rho}{\partial t} \quad (2.2)$$

The range of  $x$  is from the Schottky metalization ( $x=0$ ) to the end of the depletion region.

The electron beam is swept past the sample aperture periodically at a frequency of  $\omega/2$  as described in Chapter 1. The free carrier density and the current density can be assumed to vary as  $\exp(j\omega t)$  since there are two current pulses per modulation cycle. Equation 2.2 can thus be written as

$$\frac{\partial \tilde{J}}{\partial x} + j\omega \tilde{\rho} = 0 \quad (2.3)$$

Substituting

$$\tilde{J} = \tilde{\rho} v \quad (1.4)$$

into (2.3) yields

$$\frac{\partial \tilde{J}}{\partial x} + j\omega \frac{\tilde{J}}{v} = 0 \quad (2.4)$$

a first order differential equation relating the local current density and the local drift velocity, neglecting diffusion effects.

The homogeneous solution is

$$J = J_0 \exp(-j\omega \int_0^x \frac{dx}{v(x)}) \quad (2.5)$$

with  $J_0$  as a constant dependent on the number of injected electrons and their energy. Using Poisson's equation

$$\frac{d\tilde{E}}{dx} = \frac{\tilde{\rho}}{\epsilon} \quad (2.6)$$

and substituting into the current continuity equation

$$\frac{d}{dx} (\tilde{J} + \frac{d\tilde{E}}{dt}) = 0 \quad (2.7)$$

the total current can be defined as

$$J_{\text{terminal}} = J + \epsilon \frac{dE}{dt} \quad (2.8)$$

which, if integrated over the active region of the diode, relates the drift velocity to the measurable external circuit current. The applied voltage is assumed to be constant so the electric field can be taken to be time invariant. Thus the terminal current is given by

$$\tilde{I} = \frac{\tilde{J}_0}{L} \int_0^L \left\{ \exp \left[ -j\omega \left[ \int_0^x \frac{dx}{v(x)} \right] \right] \right\} dx \quad (2.9)$$

The preceding derivation was performed by Evans and Robson (3) to relate terminal current phase to localized drift velocity. To further simplify the measurement, samples with low doping concentrations can be used so the electric field and the velocity can be considered uniform along the sample. With a constant velocity (2.9) becomes

$$\tilde{I} = \frac{\tilde{J}_0}{L} \int_0^L \exp \left( -\frac{j\omega x}{v} \right) dx \quad (2.10)$$

which can be expressed as

$$\tilde{I} = - \frac{\tilde{J}_0}{\ell} \frac{v}{j\omega} (\exp \frac{-j\omega\ell}{v} - 1) \quad (2.11)$$

$$\begin{aligned} &= \frac{\tilde{J}_0}{\ell} \frac{v}{\omega} j (\exp \frac{-j\omega\ell}{2v} - \exp \frac{j\omega\ell}{2v}) \exp \frac{-j\omega\ell}{2v} \\ &= \tilde{J}_0 \frac{2v}{\omega\ell} \sin \frac{\omega\ell}{2v} \cdot \exp \frac{-j\omega\ell}{2v} \end{aligned}$$

$$\tilde{I} = \tilde{J}_0 (\text{sinc } \frac{\omega\ell}{2v}) \cdot \exp(\frac{-j\omega\ell}{2v}) \quad (2.12)$$

The phase of the external circuit current is

$$\phi = \frac{\omega\ell}{2v} \quad (1.6)$$

and the amplitude of the alternating current density is

$$A = |\tilde{J}_0| |\text{sinc } \frac{\omega\ell}{2v}| \quad (2.13)$$

When a bias voltage is applied to a sample under the uniform field assumption the internal electric field is equal to the voltage divided by the depletion length. From the measured current phase the velocity can be calculated using (1.6). Thus points are generated on the  $v(E)$  curve.

## 2.2 NONUNIFORM ELECTRIC FIELD SOLUTION

For samples with doping concentrations  $>5 \times 10^{14}$  the field slope will be greater than 6.8 kV/cm per micron so for a 3 or 4 micron depletion region the change in electric field can be greater than 20 kV/cm. The uniform field approximation can not be used except for areas of low mobility, where the velocity is near constant with respect to electric field.

For a given doping profile and applied voltage the electric field profile of the sample can be calculated. For a monotonically decreasing electric field the external circuit current phase can be expressed as an integral over an electric field interval on the  $v(E)$  curve instead of integrating over the depletion length. An initial guess about the  $v(E)$  curve can be made and corrected using iterative numerical methods to yield a  $v(E)$  relationship which satisfies the measured current phase. To derive such a phase- $v(E)$  relationship (2.9) must be restated in terms of the terminal current phase as

$$\phi = \text{Arg} \left\{ \int_0^{x_1} \exp \left[ -j\omega \int_0^x \frac{dx}{v(x)} \right] dx \right\} \quad (2.14)$$

where  $x_1$  is the epitaxial layer depth in the punched-through case or the point where the electric field goes to zero in non-punched through situations. See Figure 1.3. From examining the doping profile (2.14) can be changed from an integration over length to an integration over electric field.

Using Poisson's equation

$$\frac{dE}{dx} = \frac{q}{\epsilon} N_d(x) \quad (1.5)$$

the electric field profile can be described from an integration of the doping profile as in Figure 1.3 a and b:

$$E = \int \frac{q N_d(x)}{\epsilon} dx = E_0 + f(x) \quad (2.15)$$

Integrating (2.15) over the depleted region yields the applied voltage. So for a reverse bias voltage and a known doping profile the electric field vs. depth profile can be determined.

A change in the variable of integration can be made using

$$\frac{dx}{dE} = \left( \frac{q N_d(x)}{\epsilon} \right)^{-1} = h'(E) \quad (2.16)$$

$$E|_{x=\ell} = E_\ell \quad \text{punched-through} \quad (2.17a)$$

$$E|_{x=x_1} = 0 \quad \text{non-punched} \quad (2.17b)$$

The phase can therefore be expressed as

$$\phi(Va) = \text{Arg} \left\{ \int_{E_0}^{E_\ell} \exp \left[ -j\omega \int_{E_0}^{\epsilon} \frac{h'(y) dy}{v(y)} \right] h'(\epsilon) d\epsilon \right\} \quad (2.18)$$

This equation facilitates the use of numerical integration and Newton-Raphson iterative methods to determine the velocity-field

relationship. The key to understanding the analysis method used here is to recognize that each measurement describes a double integration on a specific interval of the  $v(E)$  curve.

As the electron passes through the depletion region it moves with a velocity related to the local electric field. For a given applied voltage the electric field can be determined, along with its most negative value at the metallization, and its least negative at the end of the epitaxial layer, assuming a punched-through state. Figure 2.1 illustrates a typical  $v(E)$  curve divided into measurement intervals, each with a corresponding current phase. The external current phase is a double integration on each section of the curve so a method must be used to derive the curve which best satisfies the measured phases. To perform this de-embedding, electric field intervals can be chosen to yield sufficient resolution around the  $v(E)$  curve regions of greatest mobility deviation. The integration of the curve masks information about its shape within the electric field limits. However, many integrations over different intervals can give enough information so that a correct curve can be obtained.

From lumped element modeling, which will be explained in Chapter 3, punched-through biasing was found to be the only way to perform these measurements. Samples with epitaxial layer doping concentrations on the order of  $2 \times 10^{15} \text{ cm}^{-3}$  and 3 to 5 microns in length were necessary for good analysis of the raw data. The program used for the analysis is listed in Appendix 7.1 and is described in block diagram form in Figure 2.2. A general description of its function is as follows:

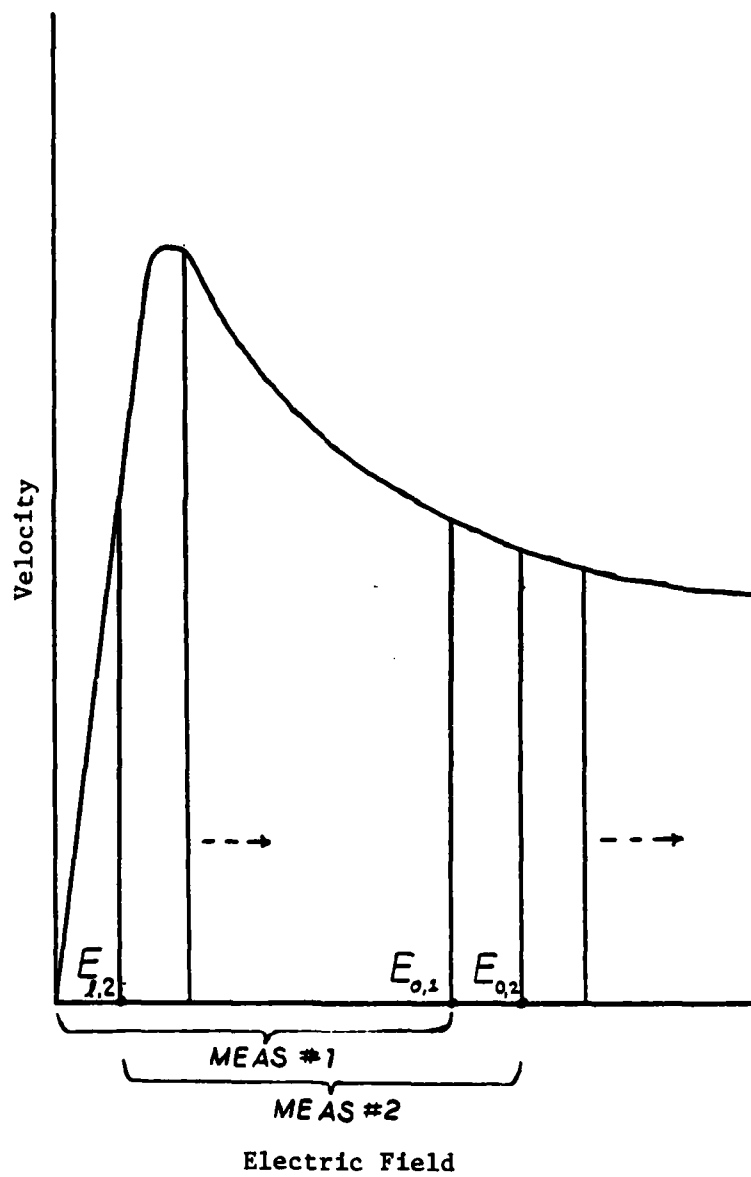


Figure 2.1 Electric field intervals for individual phase measurements



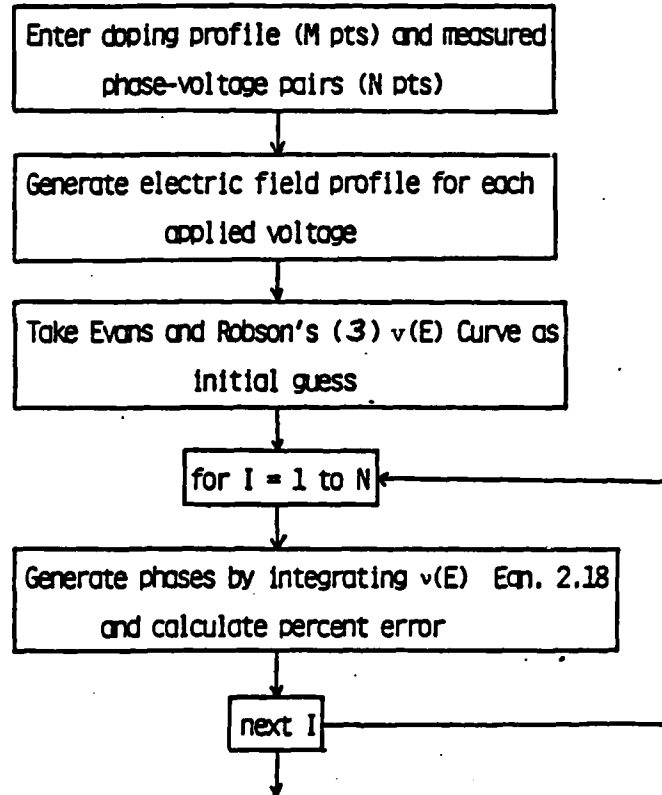


Figure 2.2 Block diagram of Newton-Raphson iterative method.

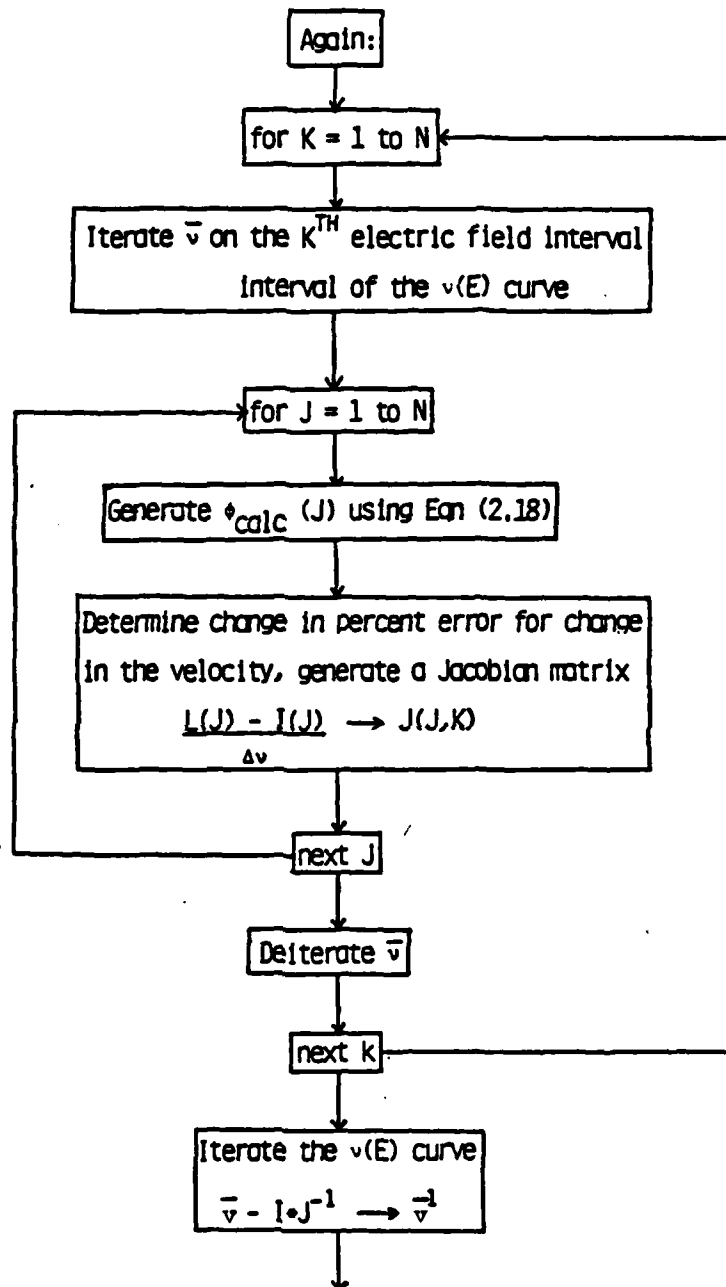


Figure 2.2 (cont.)

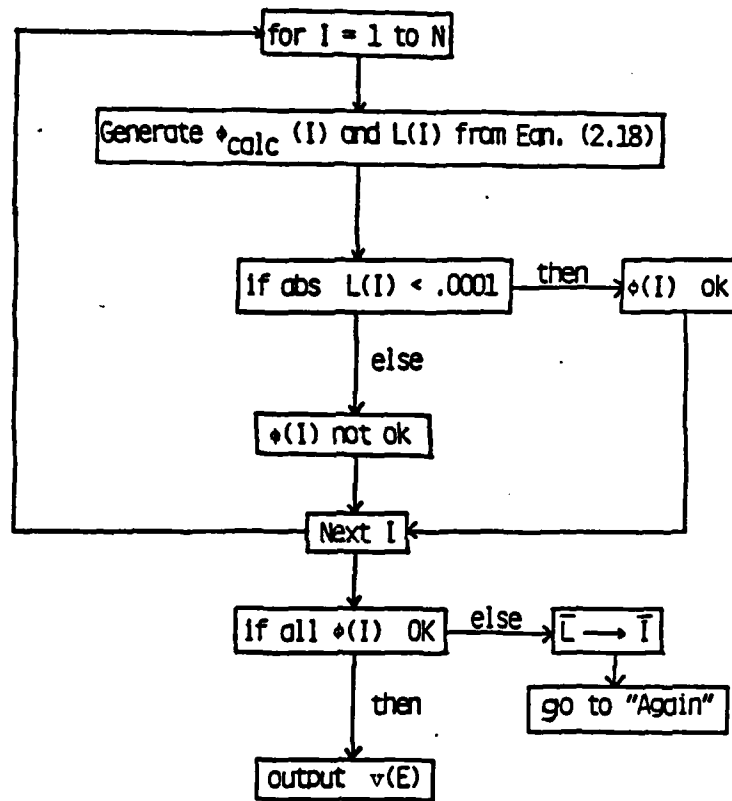


Figure 2.2 (cont.)

- a) An initial guess is made about the shape of  $v(E)$  curve and numerical integration is performed to produce the expression  $G(\epsilon)$

$$G(\epsilon) = \int_{E_0}^{\epsilon} \frac{h'(\gamma) d\gamma}{v(\gamma)} \quad (2.19)$$

- b) Euler's relation allows equation (2.18) to be represented by two integratable expressions, one real and one imaginary.

$$\phi = \text{Arg} \left\{ \int_{E_0}^{E_2} \cos(\omega G(\epsilon)) h'(\epsilon) d\epsilon - j \sin(\omega G(\epsilon)) h'(\epsilon) d\epsilon \right\} \quad (2.20)$$

- c) After integration the half angle relation is used to find the calculated phase and a percentage error,  $L$ , is found between the measured and the calculated phase values.

$$L = \frac{\phi_{\text{meas}} - \phi_{\text{calc}}}{\phi_{\text{meas}}} \quad (2.21)$$

- d) A measurement electric field interval on the  $v(E)$  curve is incremented by a constant velocity step across the range. Steps a) through c) are then repeated and the change in percent phase error for the velocity increment can be found for each measured point. This interval incrementing is done for each measurement with the percent error changes calculated for all the phases each time until a Jacobian matrix,  $J$ , is generated.

The velocity-field curve is then augmented by

$$\bar{v}' = \bar{v} - \bar{I} * \bar{J}^{-1} \quad (2.22)$$

where the I matrix is the percentage difference between the measured phase and the phase calculated from the previous  $v(E)$  curve.

- e) Steps a) through d) are repeated, iterating the  $v(E)$  guess each time, until the percentage error for each measured point falls below some minimum value. The resulting velocity-field curve is then the unique solution for the measured data.

The above method assumes zero diffusion, no phase ambiguity, and accurate phase measurements. Diffusion was neglected primarily because the analysis becomes too difficult otherwise. The sample lengths were kept short to minimize diffusion effects on the phase of the detected signal. This method can be used for any  $v(E)$  relation and any semiconductor where diffusion is not too great (<15% phase inaccuracy).

The accuracy of the raw phase-voltage data limits the accuracy of any measurement technique. Therefore a system had to be designed to generate reliable raw data. Chapter 3 describes the hardware used in this scheme to produce useful phase vs. voltage measurements.

### 3. SYSTEM REALIZATION

Performing the phase vs. applied voltage measurements requires a dependable carrier injection and current phase detection system. Each part of this system had to be fabricated and individually tested to meet our specific criteria of performance and reproducibility. A detailed description of the electron gun, power supply and second stage amplifier is available to the reader in O.N.R. Report #80-2 (8). Machine drawings for certain sub-systems and circuit diagrams for the power supply can be found here in the appendices. Figure 1.5 is a block diagram of the entire apparatus. The following sections describe the operation of the individual sub-systems.

#### 3.1 ELECTRON GUN AND POWER SUPPLY

A means of injecting a large number of free carriers into the depletion region of the Schottky diode had to be designed with high stability and minimal unwanted modulation. Electron beam injection was chosen since the technology is well known and the technique is applicable to almost all semiconductor materials. Constant beam position with varying beam potential or beam penetration into the sample is also desired.

Figure 3.1 shows a sketch of the HP 500 MHz oscilloscope gun used as the electron source. The potentials relative to the mesh cup are indicated. The filament is a thoriated tungsten wire mounted on a ceramic standoff within the grid cup. The indicated potentials were chosen to give the highest beam current density at the sample target.

In anticipation of making measurements at two different frequencies the vertical deflection plates were used as a second modulator. These plates are actually a helical ribbon pair designed to have a 300 ohm characteristic impedance up to 500 MHz. In order to drive the vertical modulator a 300 ohm transmission line was implemented using two nickel wires separated by teflon spacers. Modulation power was coupled to the vertical pins on the gun connector through a bifilar wrapped toroid which provides isolation and impedance matching. Modulation at 500 MHz was observed on a phosphor target as shown in Figure 3.2 and a 1 GHz signal was detected through a sample diode.

The filament of the gun is held at a voltage much lower than that of the sample target which is at earth ground. The special negative high voltage power supply shown in Figure 3.3 had to be built for this experiment.

Two supplies were used to give a constant voltage difference across the zener diode and resistor chain used to obtain all the required gun potentials. This allowed the pick off points to be maintained at the same voltage relative to the reference for a variable beam potential. High voltage supply #1 is an adjustable

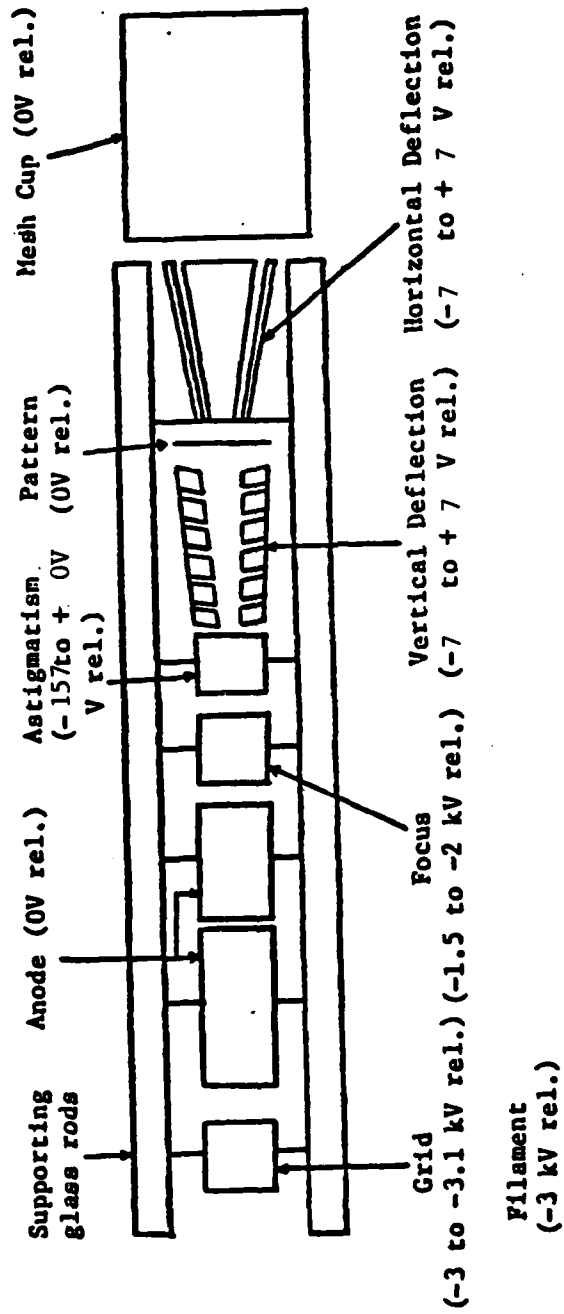
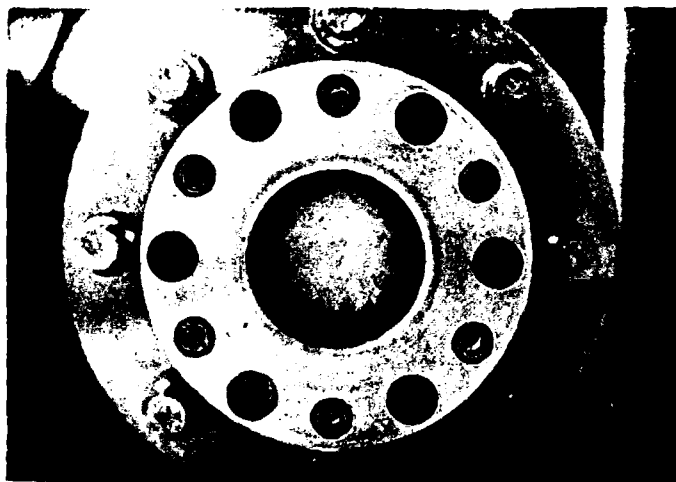
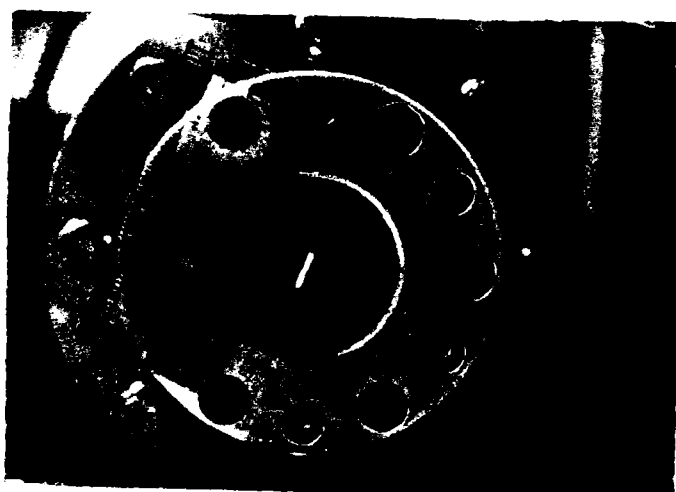


Figure 3.1 Electron gun (all voltages relative to accelerating potential)

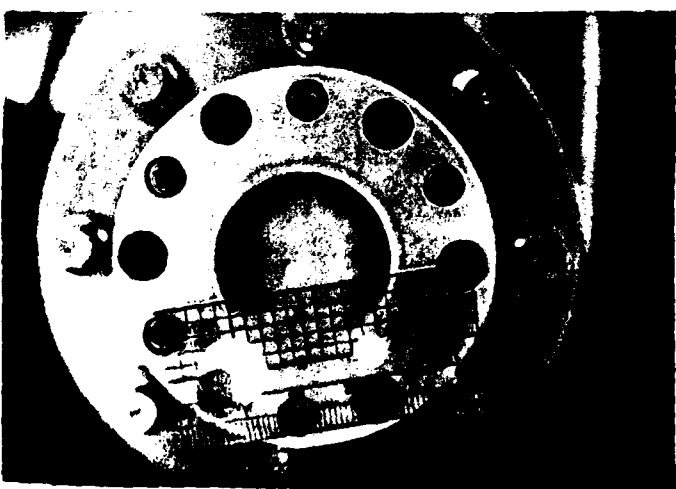




BEAM PATTERN  
NO MODULATION



VERTICAL  
DEFLECTION  
500 MHz



HORIZONTAL  
DEFLECTION  
6 GHz

Figure 3.2 Beam Modulation observed on a phosphor target



reference using negative feedback for regulation. The output of the flyback transformer labeled HV#1 is fed back through a 500 Megohm series resistance to the negative input of a 741 operational amplifier which regulates the amplitude of the current spikes from the switching circuit through the transformer. The 500 Megohm resistance and 17.6 nF capacitance in shunt with the flybacks provide sufficient smoothing of the high voltage waveform.

The second high voltage supply is identical to the first except its input maintains HV#2 at a fixed potential offset from HV#1, usually by -2.8 kV. Both transformer switching circuits run off the same asynchronous 15 kHz signal to eliminate uncoordinated ripple in the high voltage output. The flybacks and smoothing circuits are housed in aluminum boxes and coaxial switching circuit lines are used to minimize electromagnetic pickup on the gun controls. The entire supply is floating so a high value resistor placed between floating ground and earth ground can be used to indicate the beam current passing through the final beam aperture.

The filament supply circuit board is similar in layout to the switching circuit board used for the high voltage supplies and is also timed with the HV switching waveform. The spiky current passes through the primary winding of an isolation transformer, which is also electrically shielded, whose secondary is within 100 V of HV#2 potential. The secondary signal is then fullwave rectified and smoothed to provide two amps DC current to the filament which has a cold resistance of about one ohm. There is virtually no observable density modulation on the electron beam.

The pickoff chain as seen in Figure 3.3 was chosen for ease of operation and optimum DC beam current through the sample. With one plate of both horizontal and vertical deflection tied to reference a plus or minus seven volt swing on the opposite plate gave adequate deflection with the right amount of sensitivity on the control knob. Astigmatism and focus were chosen through observation for best beam geometry and the filament and grid potentials were picked so the grid had enough negative offset to shut off the electron beam completely.

Figure 1.5 shows the electron gun and power supply configuration with the rest of the system. The gun is placed in a pyrex tube which is painted both inside and out with conducting paint (an Aquadag E and sodium silicate mixture) to prevent static charge build-up on the tube surfaces. The interior coating is tied to HV reference while the exterior is at earth ground. The gun and all related surfaces exposed to hard vacuum were cleaned with TCE, acetone and isopropyl alcohol before pumping. The pyrex tube forms the vacuum jacket of the apparatus.

The resulting electron beam is 350 nanoamps with a diameter on the order of 30 mils. The range of beam potential is 3kV to 18kV, but the usual operating point is 6.75kV. The 500 MHz modulator provides half an inch deflection on a phosphor target with half a watt incident on the bifilar wrapped transformer of the vertical deflection input.

### 3.2 6 GHz MODULATOR

High frequency modulation of the charge carrier density in the active region of the sample is required to get enough phase resolution to derive the velocity-field relationship. Calculations have shown that for a diode with a 4  $\mu\text{m}$  epitaxial layer, 12 GHz will provide sufficient phase difference for the HP ANA to produce accurate measurements in the electric field regions of interest (8). A 6 GHz modulator was therefore required which would produce adequate transverse deflection at the sample.

For convenience and effective operation a reentrant coaxial cavity modulator as shown in Figure 3.4 was designed. The modulator body element consists of a cylindrical bore in its center to form the outer wall of the resonator. A conducting center post is located coaxially within the bore. This configuration looks like a section of coaxial transmission line near a quarter of a wavelength at 6 GHz. Figure 3.5 illustrates the radial standing wave pattern within the coax. The ported end at the bottom appears as a low impedance and the beam aperture appears to be capacitively loaded, close to an open circuit. This cavity resonates at 6 GHz and the electric field between the post and the top of the cavity is nearly vertical as shown in Figure 3.5. Coupling to the resonator is provided by an iris at the end of a section of ridged waveguide as seen in Figure 3.4.

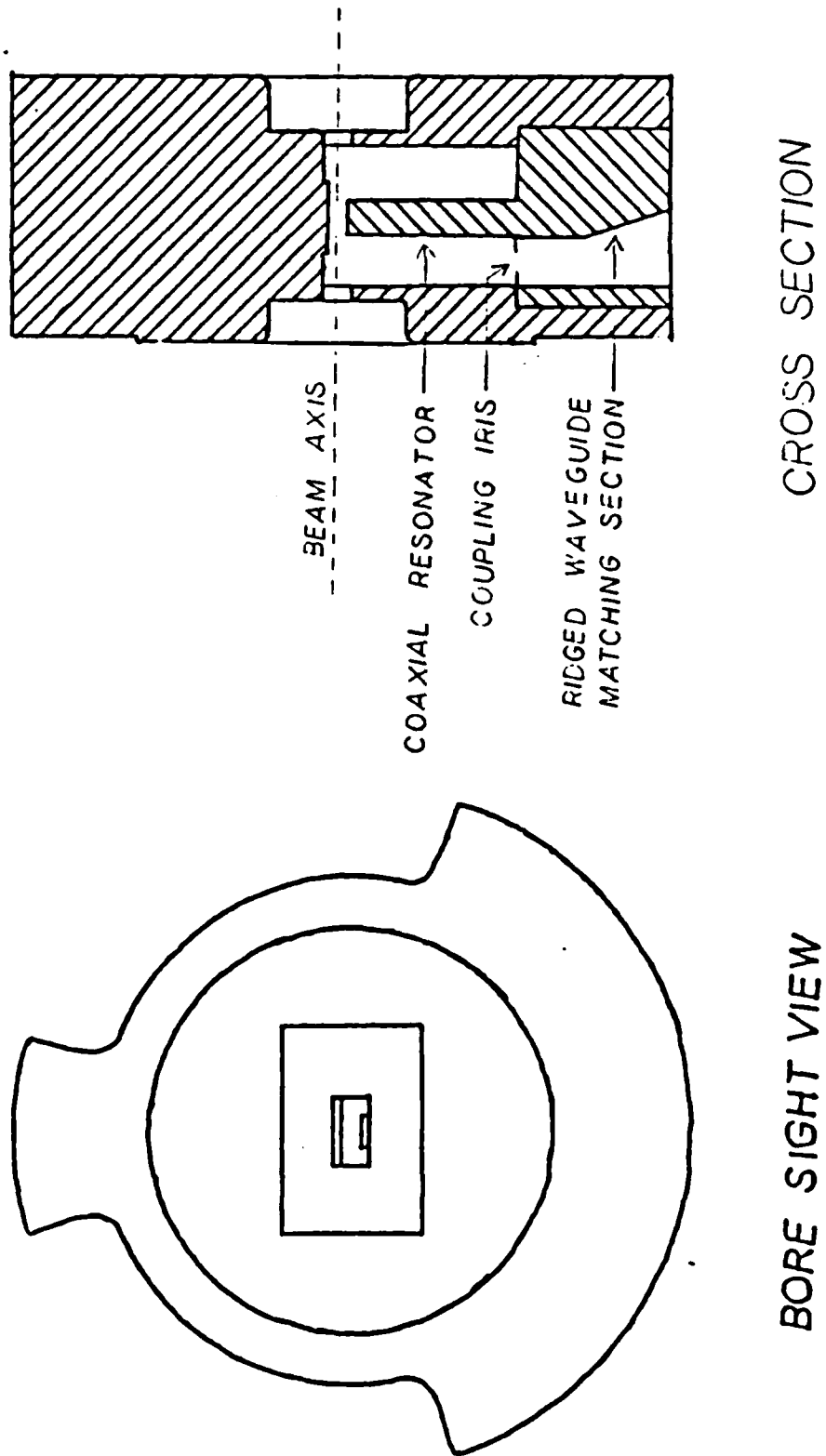


Figure 3.4 Reentrant coaxial cavity modulator body

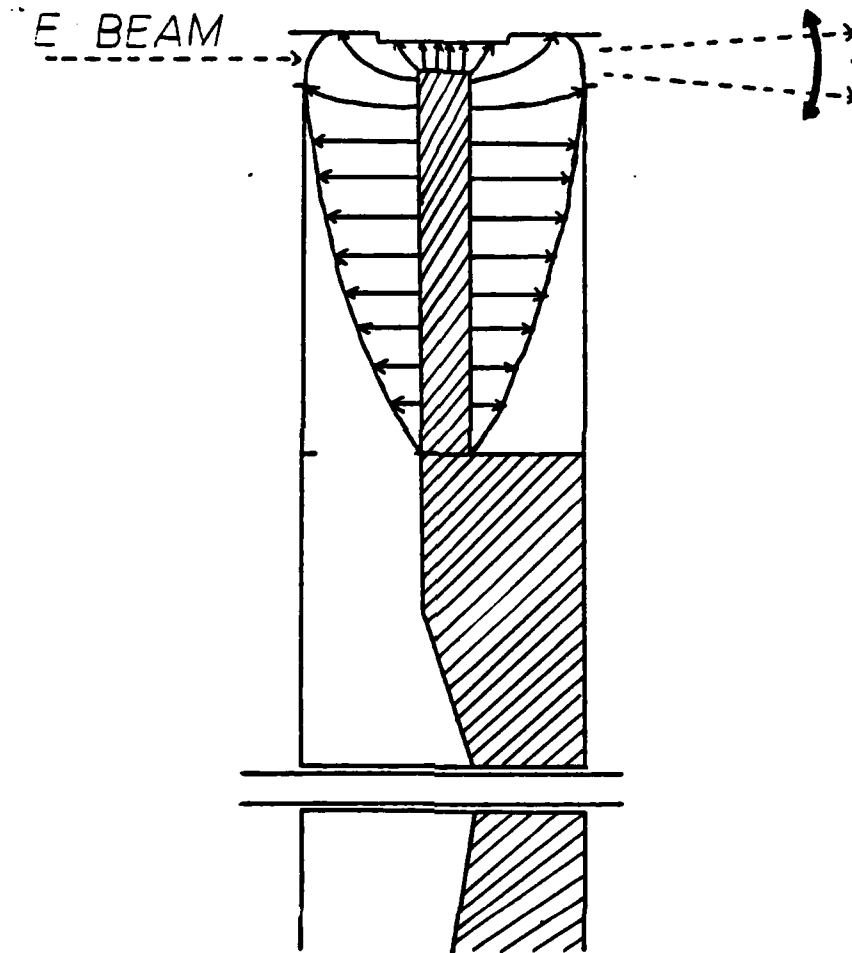


Figure 3.5 E field profile in reentrant coaxial cavity

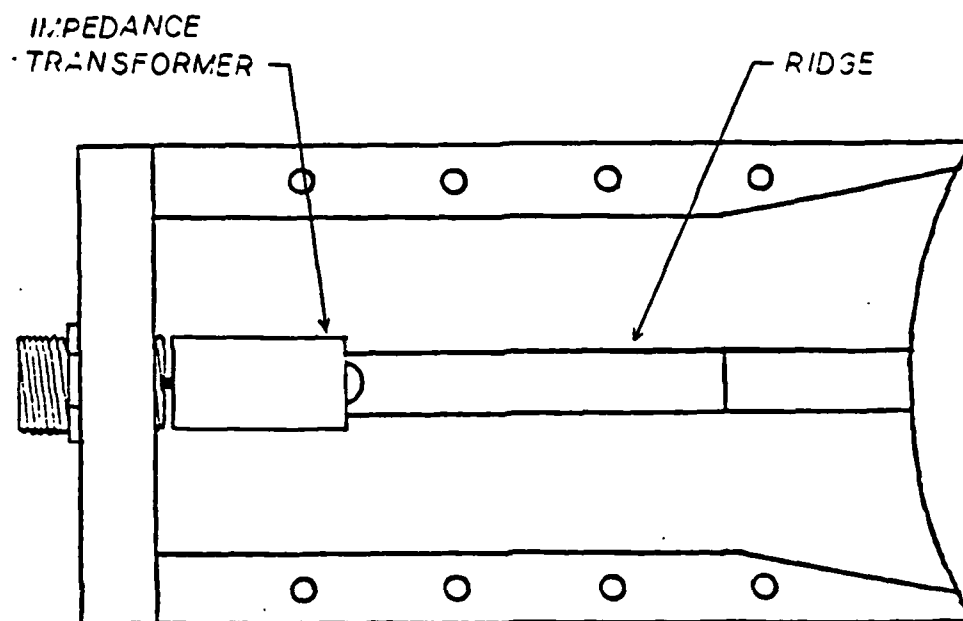
The modulator snaps into place in the mesh cup and is held at HV reference. Its edges are rounded to minimize arcing and the outer conductor walls of the coax at the aperture were narrowed to increase the angle of acceptance of the electron beam. Notches were made in the modulator perimeter to improve vacuum pumping and the body was gold plated to reduce secondary emission.

Coupling to the modulator was done through the pyrex tube wall with a ridged waveguide horn. Figure 3.6 shows the ridged waveguide launcher used. A 50 ohm coaxial probe attached to the ridge 0.25 inches long (a quarter wavelength at 6GHz) coupled the 6 GHz signal to the waveguide from coaxial input. The characteristic impedance of the guide is about 140 ohms so a brass slab air stripline center conductor was used to make a 90 ohm, quarter wavelength, transformer to improve the match between the 50 ohm coax and the ridged waveguide.

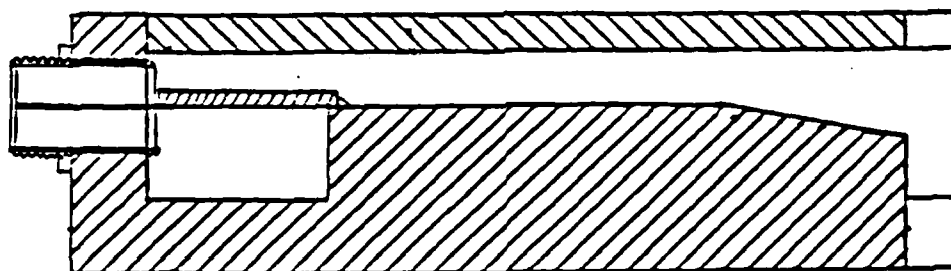
The mouth of the launcher and the modulator were flared to improve power transmission through the pyrex. Both pieces were machined to mate flush with the tube wall.

At resonance, the return loss was measured at -16 dB at the launcher input. The 6 GHz deflection system provides from a tenth to a fifth of an inch deflection at the sample with half a watt incident on the launcher, as can be seen in Figure 3.2. Power is provided by a 6 GHz Gunn oscillator with an attenuator to maximize the 12 GHz component in the detected sample signal and an isolator to minimize frequency drift from load variation. Detectable 12 GHz signals were obtained with modulation power as low as 5 mW.





TOP VIEW-LID OFF



CROSS SECTION

Figure 3.6 6 GHz waveguide launcher

### 3.3 SAMPLE AND SAMPLE HOLDER ASSEMBLY

The target sample used in this system is a reverse biased Schottky diode. Figure 3.7 shows a sample cross section. On a highly doped substrate approximately 100 microns thick a 2 micron buffer with doping concentration on the order  $10^{17} \text{ cm}^{-3}$  is grown to prevent back diffusion of dopant during epitaxial growth. An epitaxial layer is then grown between 2 and 5 microns thick with doping in the range of  $4 \times 10^{14}$  and  $2 \times 10^{15} \text{ cm}^{-3}$ .

The Schottky barrier consists of a 0.025 inch diameter, 200 Å thick circle of aluminum evaporated on the epitaxial surface. To penetrate this metallization requires approximately one keV of beam energy (7) so the energy of the beam within the material still far exceeds the band gap energy of the semiconductor. This excess energy is expended in the generation of electron-hole pairs within the first half micron of the depletion region. Current multiplication on the order of a thousand has been observed, boosting the detected 12 GHz signal by approximately 30 dB. A 0.005 inch wide, 7000 Å thick guard ring was also evaporated on top of the circle for bond wire contact to the conventional C3 package used to mount the sample in the measurement system. On later samples a bond pad, 0.002 inches by 0.002 inches, was used in place of the guard ring as the bonding area. More current was detected since the area of the thin metallization was increased significantly, increasing the number of energetic electrons penetrating into the depletion

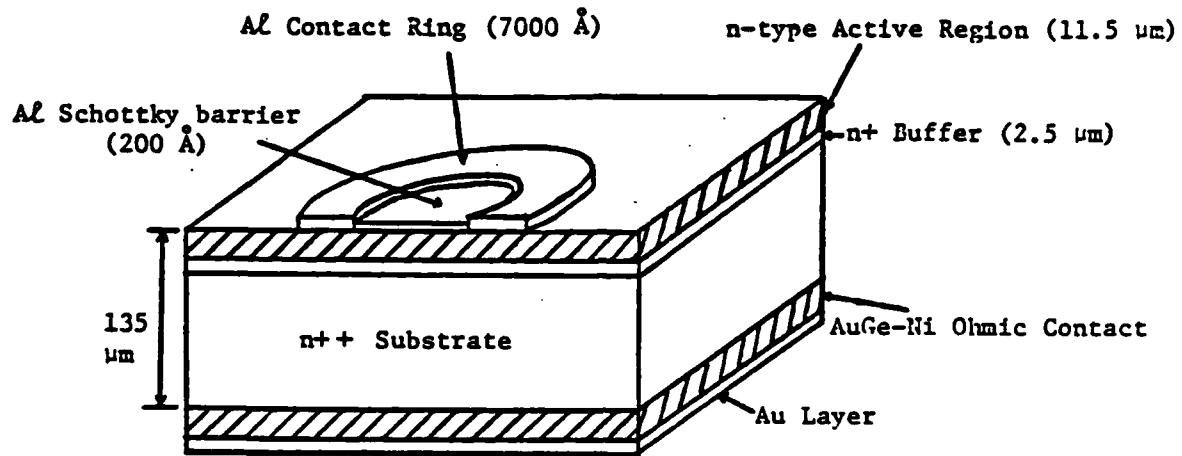


Figure 3.7 GaAs Schottky barrier sample

region. Bond wires 0.001 inch in diameter are used to contact the bond area to the C3 package.

On the anode side of the diode an AuGe-Ni and Au ohmic contact is made. This low resistivity contact is then soldered to the center post of the C3 diode package. Figure 3.8 shows a packaged diode mounted on the center post. Parasitic impedances must be examined to understand the phase characteristics of the packaged sample.

Figure 3.9 shows the lumped element model for the measurement sample. The current source,  $I_A$ , is the induced current due to charge carrier motion through the sample. The bond wire inductance,  $L_b$ , is estimated to be 0.75 nH for two parallel bond wires. Package capacitance,  $C_p$ , for the C3 package is about 0.024 pF. The load impedance,  $Z_L$ , shown is a combination of the fringing capacitance of the mount and the detection circuit input impedance as seen at the plane of the diode mount. All of the passive elements are constant with bias except the ring capacitance. The inactive region beneath the bonding area looks like a parallel plate capacitor whose capacitance decreases with increasing reverse bias. The ring region is inactive since the thick metallization prevents charge from penetrating into the depletion region beneath the bonding surface. At, or close, to punch-through the ring capacitance can be assumed to be constant. Previous measurements attempts were made at punch-through so varying parasitic capacitance was not a factor. Understanding of the effect of packaging parasitics, however, is

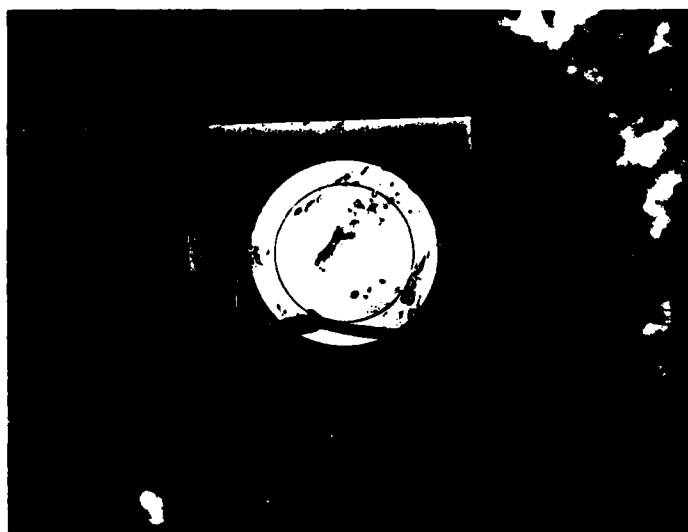


Figure 3.8 Photograph of a packaged GaAs sample

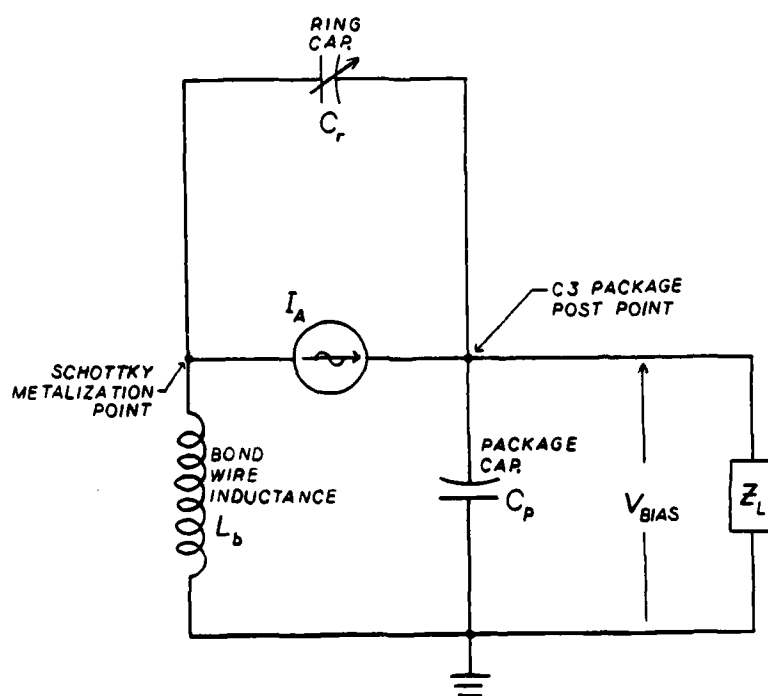


Figure 3.9 Lumped element representation of the packaged sample with an injected, modulated beam.

necessary in the interpretation of the external current phase-voltage relationship.

Appendix 7.4 shows the analysis used to derive the following relationship between the current source to be determined and the detected signal

$$V_m = \frac{Z_L I_A}{1 - \omega^2 C_r L_b + j\omega Z_L (C_p + C_r - \omega^2 C_p C_r L_b)} \quad (3.1)$$

This equation shows that for a constant ring capacitance ( $C_r$ ) the phase of the impedance multiplication factor is constant. Accurate measurements must therefore be done at or near punch through to minimize circuit related phase variation. This also suggests that calibration with an empty C3 package would be futile since the phase of the parasitic circuit would not be taken properly into account. If the velocity is assumed to go to zero as the electric field does then a reference point is achieved for these measurements. Calibration depending on other data is therefore unnecessary.

The packaged diode is placed in the sample holder as shown in Figure 3.10. From sample capacitance vs. voltage measurements and from estimations of the bond wire inductance it was determined that the source impedance of the diode was on the order of j5 ohms. To better match the diode to the 50 ohm impedance of the measurement system a 15 ohm quarter-wave transformer was incorporated into the holder. Teflon dielectric loading was used to reduce the physical length of the transformer and to act as a stand off to prevent contact to the outer conductor wall. The center conductor of an SMA

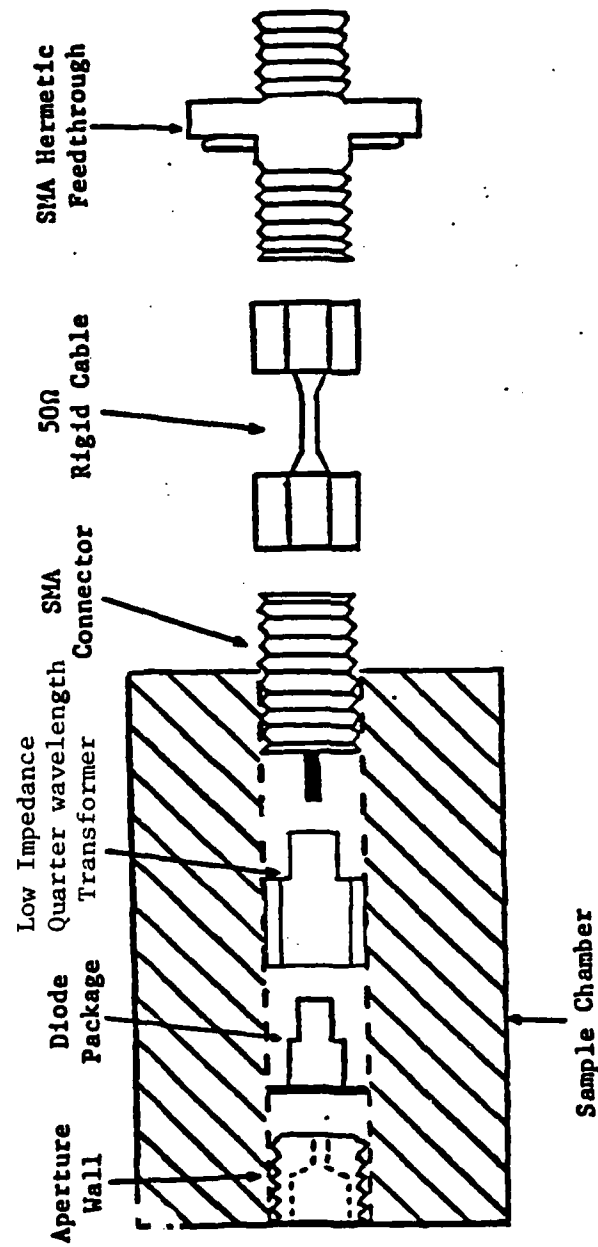


Figure 3.10 Assembly of sample holder transmission line



connector was soldered to the transformer and its outer conductor soldered to the copper sample chamber. The detected 12 GHz signal improved greatly with the introduction of the transformer.

The sample chamber mounted to the vacuum flange is pictured in Figure 3.11. The diode package is placed into the mount and an aperture wall is screwed in to make good contact with the diode package. The RF/bias feedthrough can be seen making contact to the back of the sample holder: the pipes which support the holder are also shown. These pipes lead to a hollow cavity around the sample chamber, through which hot or cold fluids can be pumped to regulate sample temperature. Figure 3.12 shows the assembly mounted on the far side of the vacuum tee.

### 3.4 DC CHARACTERIZATION OF THE APPARATUS

In order to determine the performance of the system several DC measurements were done on both the sample and a blank C3 package. Performance curves were generated to help understand any differences from predicted behavior of the injection or detection scheme. The samples used in these experiments were GaAs Schottky diodes.

Detected current vs. beam potential is shown in Figure 3.13. The lower trace is the maximum current that could be obtained through the blank package and the upper curve is for a Schottky sample. Both have a peak about -6.5 kV which is expected since this is near the operating point and all the gun potentials were adjusted -

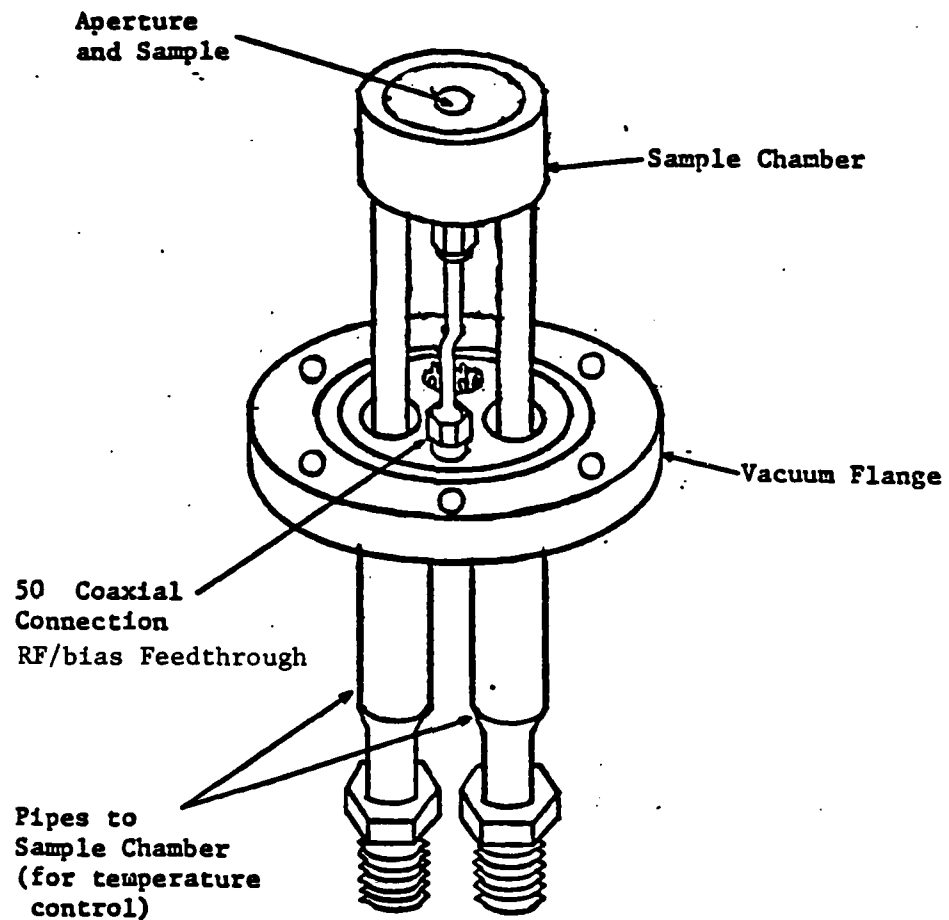


Figure 3.11 Sample holder assembly

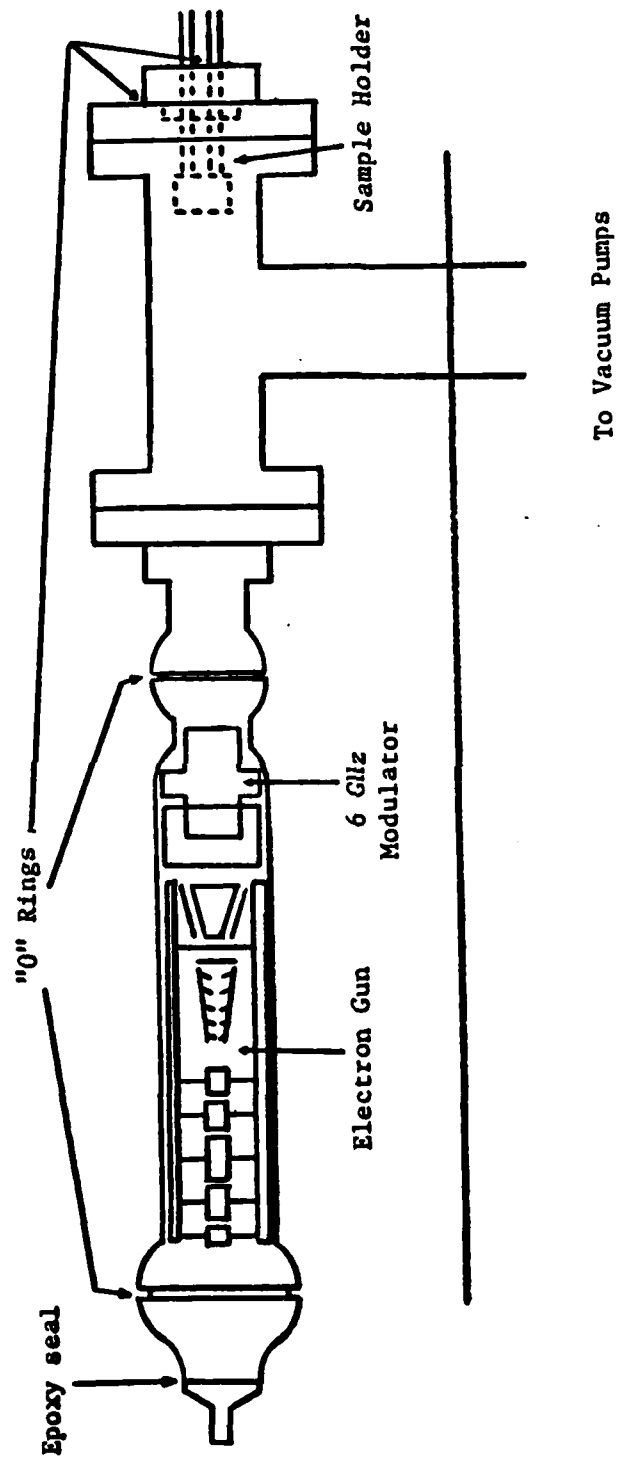


Figure 3.12 Vacuum envelope assembly

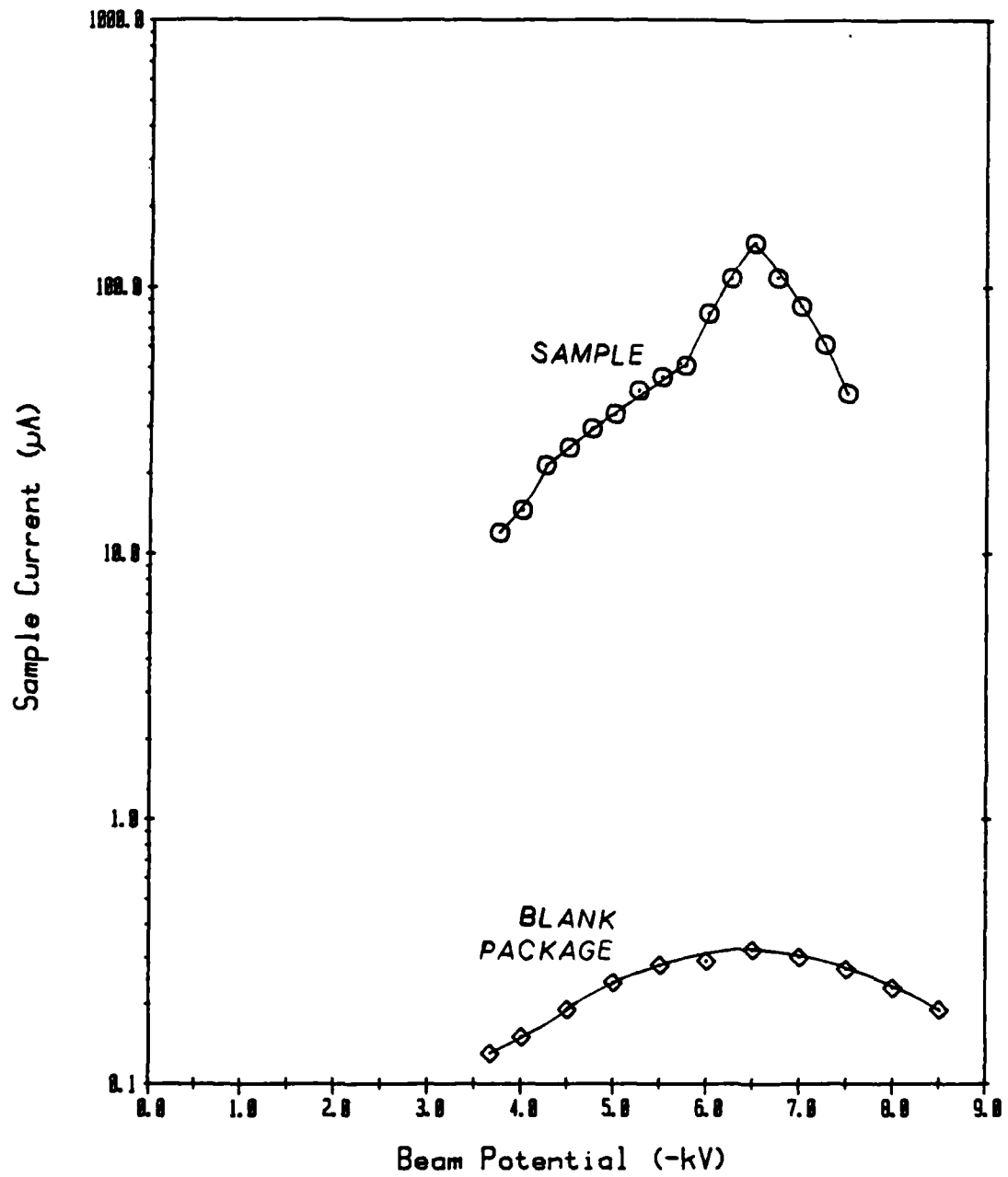


Figure 3.13 Detected current vs. beam potential

for maximum current density at this point. The ratio of the sample current to the blank current is the current multiplication factor. Figure 3.14 shows its experimental relationship to beam potential. Since the area of beam acceptance of the sample is less than half that of the empty package the peak should be at the point of focus on the sample face. The multiplication factor peak is therefore due to most of the electron beam crowding into the narrow (0.02 inch diameter) circle that is the sample target. Division of the beam energy by the band gap energy would lead to an estimate of the current multiplication of several thousand.

Reverse bias measurements were performed on the sample to estimate the limit on the system by operating the Schottky diode at high bias. Figure 3.15 shows the measured leakage current of the sample with no electron injection. The upper trace is the maximum current available through the sample with a -6.75 kV electron beam incident. If the leakage current is subtracted from the sample current the resultant current due to injected carrier excitation looks nearly independent of the bias. Figure 3.16 shows this result. This is understandable as the generation of electron hole pairs which determines the carriers available is independent of the reverse bias. The increase seen at -36 V is probably from avalanche gain in the presence of injected carriers.

These results indicate that the injection system and sample were operating properly. A beam current of 330 nA was measured; however detecting the RF was much more difficult.

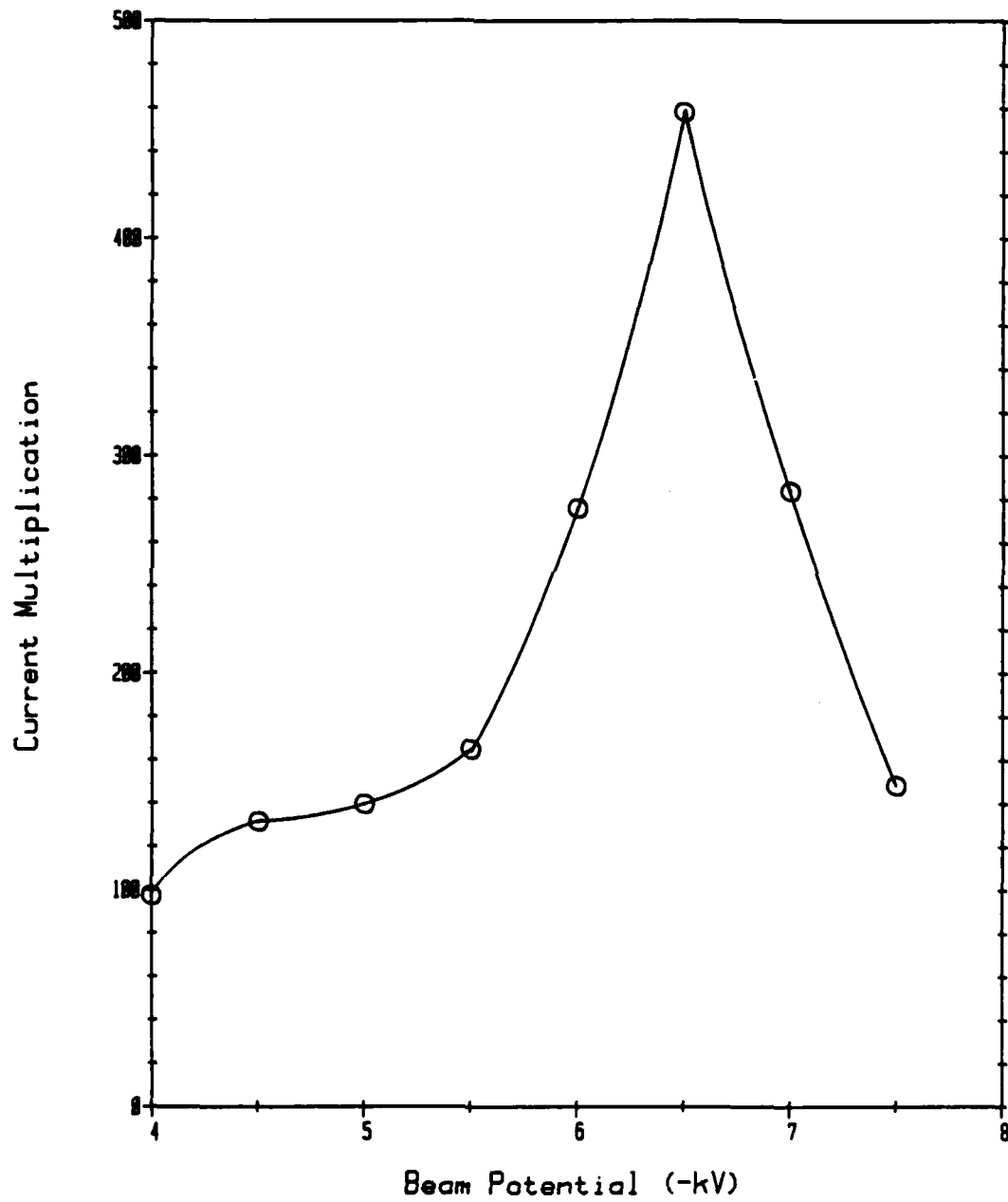


Figure 3.14 Current multiplication vs. beam potential

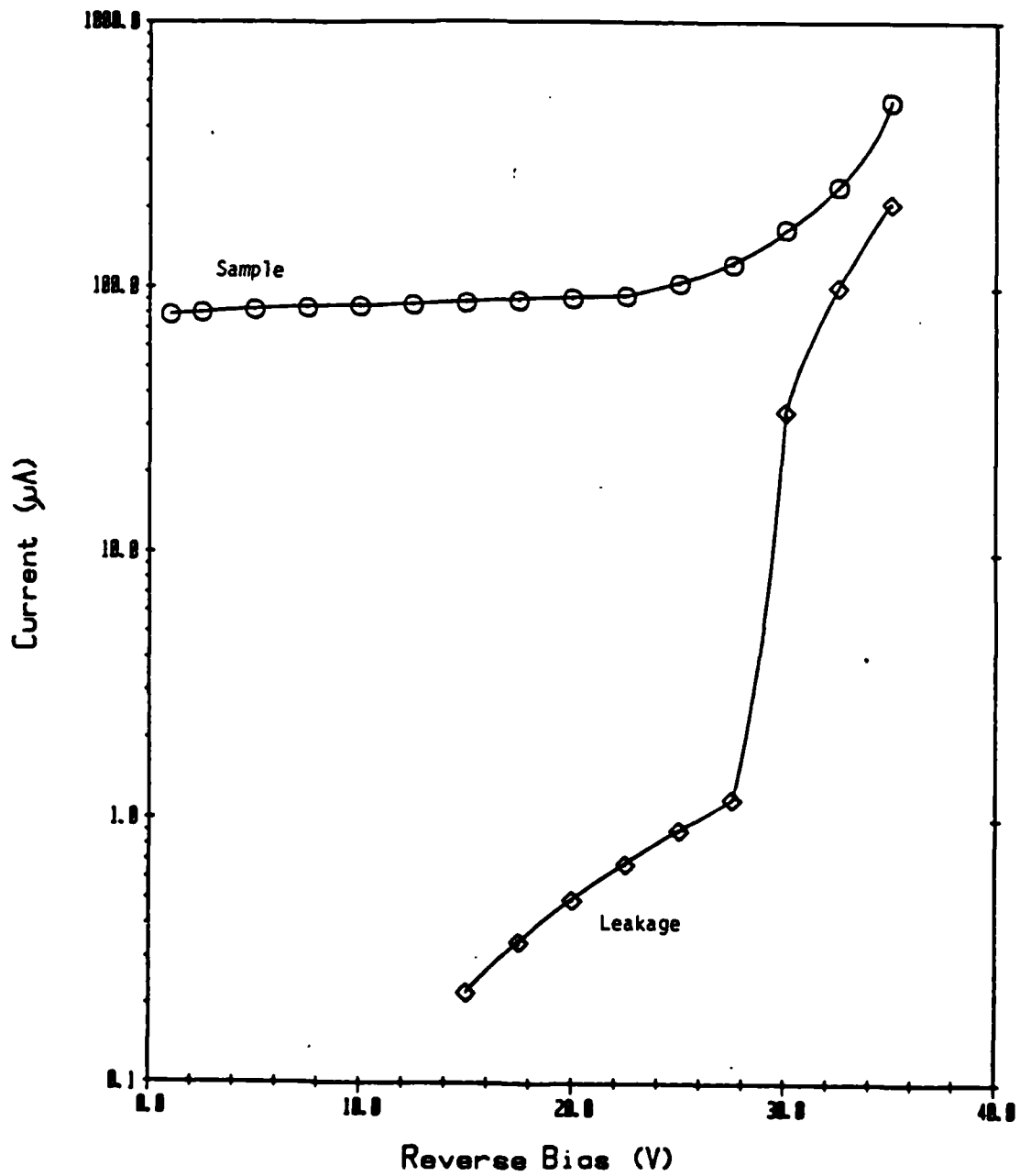


Figure 3.15 Sample current vs. reverse bias

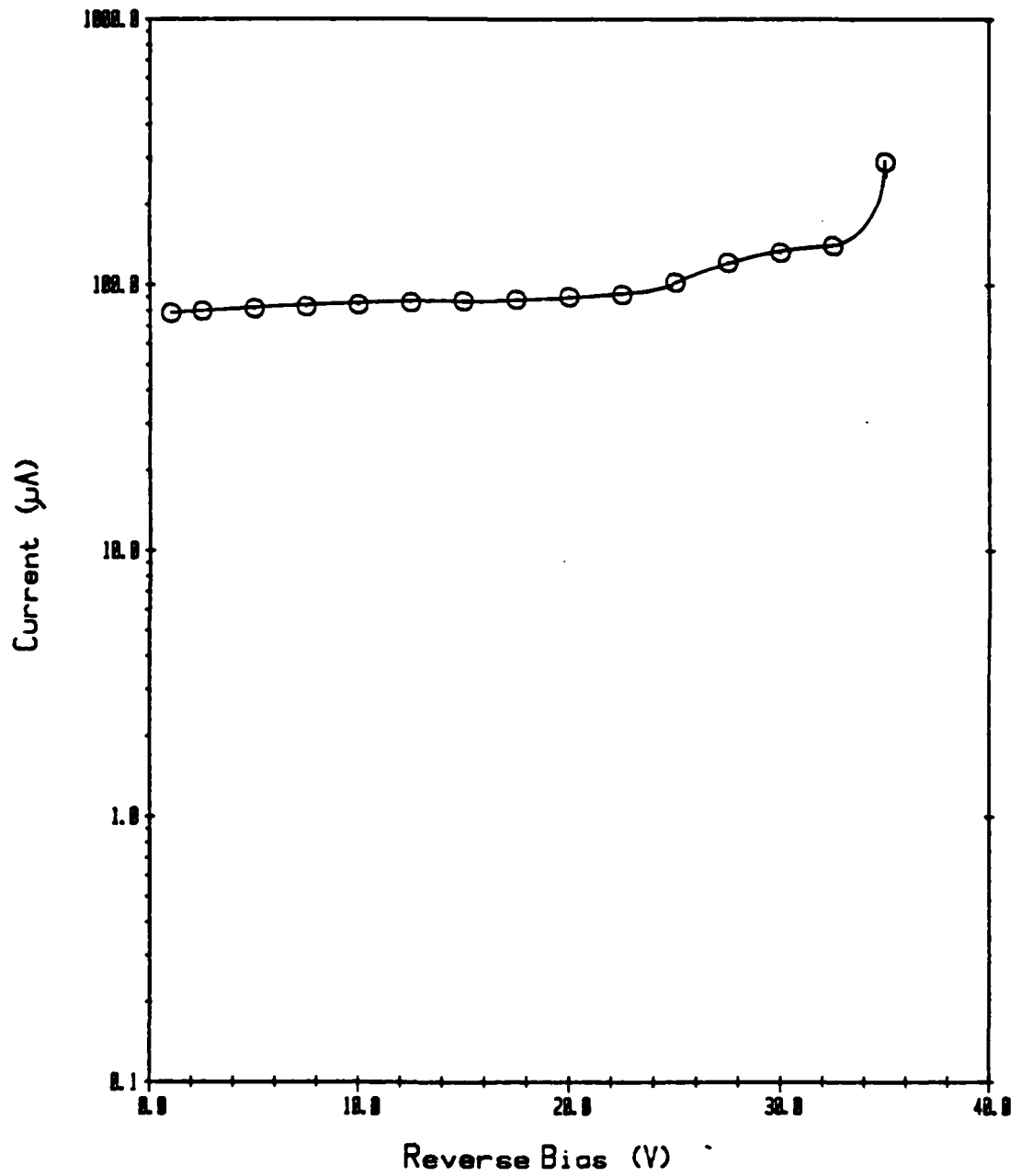


Figure 3.16 Beam induced current vs. reverse bias



### 3.5 TUNING AND AMPLIFICATION OF THE DETECTED SIGNAL

#### 3.5.1 Double Stub Tuner

To maximize the test signal power detected some tuning had to be provided to improve the match between the source impedance of the sample, in the sample holder, and the input to the first stage amplifier. A tuner was needed which would transmit DC for sample bias and minimize second harmonic pickup from the 6 GHz source. The detected signal is about -70 dBm so pickup of the 12 GHz frequency at this level will be noticable.

The tuner used was a 50 ohm airline about four wavelengths long at 12 GHz with two 25 ohm quarter wavelength slugs on the center conductor. These slugs were free to slide along the center conductor to provide the proper impedance transformation for maximum signal power. Holes were drilled and tapped in the slug walls for plastic screws which protruded through a slot in the outer conductor. These screws were used both to adjust position and as set screws to fix the slugs in place. This slot in the tuner body was covered with a piece of Ecosorb with a slit along the airline axis to accomodate the set screws. Type N connectors were used at the tuner ends. The tuner performed adequately with little unwanted pickup. Machine drawings of the body, center conductor and tuning slugs are in Appendix 2.

### 3.5.2 Cascaded Amplifiers

The detected signal from the sample diode can be as low as -75 dBm. The HP 8411A harmonic converter has a detection threshold of -70 dBm. So low noise amplification was needed to provide adequate signal for phase detection. In this system two narrow-band, low noise amplifiers were used to raise the signal to about -25 dBm.

The first stage is an 11.75 to 12.25 GHz FET amplifier with 28 dB gain across the band and a 4 dB noise figure. The unit was specially made with a bias tee on the input for sample diode biasing. No separate bias tee is needed.

The second stage is also an FET amplifier with 20 dB gain over 11.25 to 12.2 GHz with a noise figure below 6 dB. The two stages together provide about 45 dB of gain with a noise figure of 6 dB.

### 3.6 MEASUREMENT SCHEME

The measurement circuit shown in Figure 3.17 is the one used to determine the phase vs. applied voltage relationship for the injected Schottky diode. The modulation signal is doubled and taken as a reference signal for the ANA. The electron beam is modulated and generates charge carriers in the target material inducing a 12 GHz current in the external circuit. This test signal is monitored with a wavemeter to measure signal frequency and a spectrum analyzer

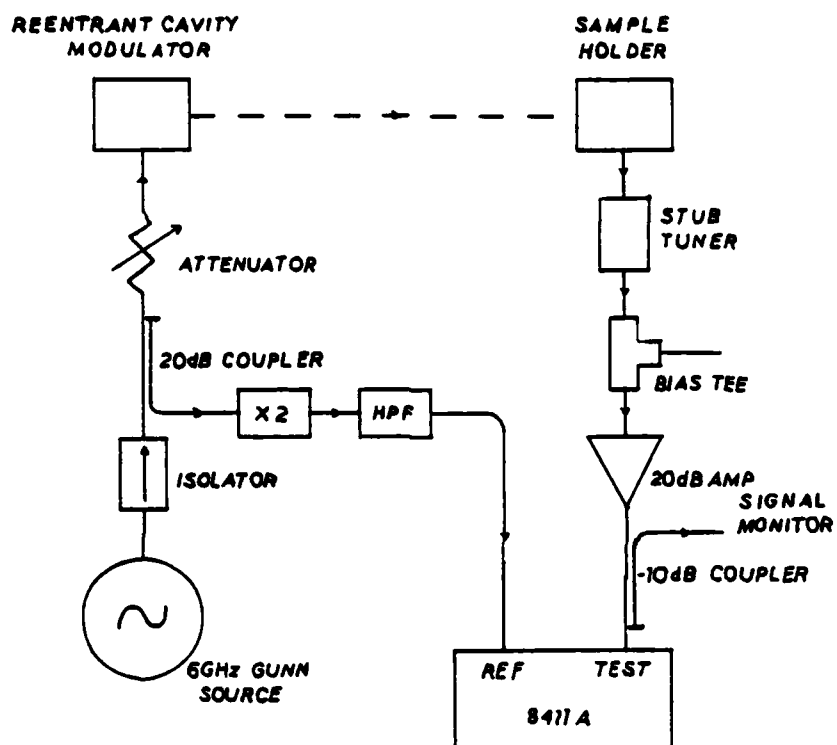


Figure 3.17 6 GHz Measurement circuit

to observe the signal level. The sample is biased by means of a precision step voltage supply to increase the measurement speed and decrease phase drift effects due to beam voltage variation with time.

Extrapolation to zero velocity was used so calibration was not necessary. These measurements were done totally under computer control which generates a phase vs. voltage table. The numbers are then entered into the numerical analysis program which iterates Evans and Robson's results (3) and generates a velocity-field curve which satisfies the raw data.

Data taken with this technique is presented in Chapter 4.

#### 4. RESULTS

##### 4.1 MEASURED RESULTS

Using the method and apparatus described in the preceeding chapters, the phase vs. reverse bias relationship was examined for a GaAs sample. The samples used were Schottky diodes, labelled 2A26 material, with a thin circular metallization, 0.025 inches in diameter, and a small square bond pad, 0.002 x 0.002 inches, for contact to the package terminal. The capacitance vs. reverse bias analysis of the material before packaging yielded the curve in Figure 4.1. From this curve the doping profile was determined, as illustrated in Figure 4.2. The epitaxial layer was found to be 1.6 microns thick with a doping concentration of about  $4 \times 10^{15} \text{ cm}^{-3}$  so only a small voltage, about 6.5 V, was needed to punch through the epitaxially grown region. Also shown is the doping profile for a second sample, M13. Figure 4.3 shows the calculated internal electric field profile for the reverse bias values shown.

To test the Schottky contact, I-V curves, such as Figure 4.4, were measured to examine the limits of reverse bias and the quality of the diodes. Very leaky contacts could not be used. The most frequent cause of failed samples was bad bond wire contacts on the

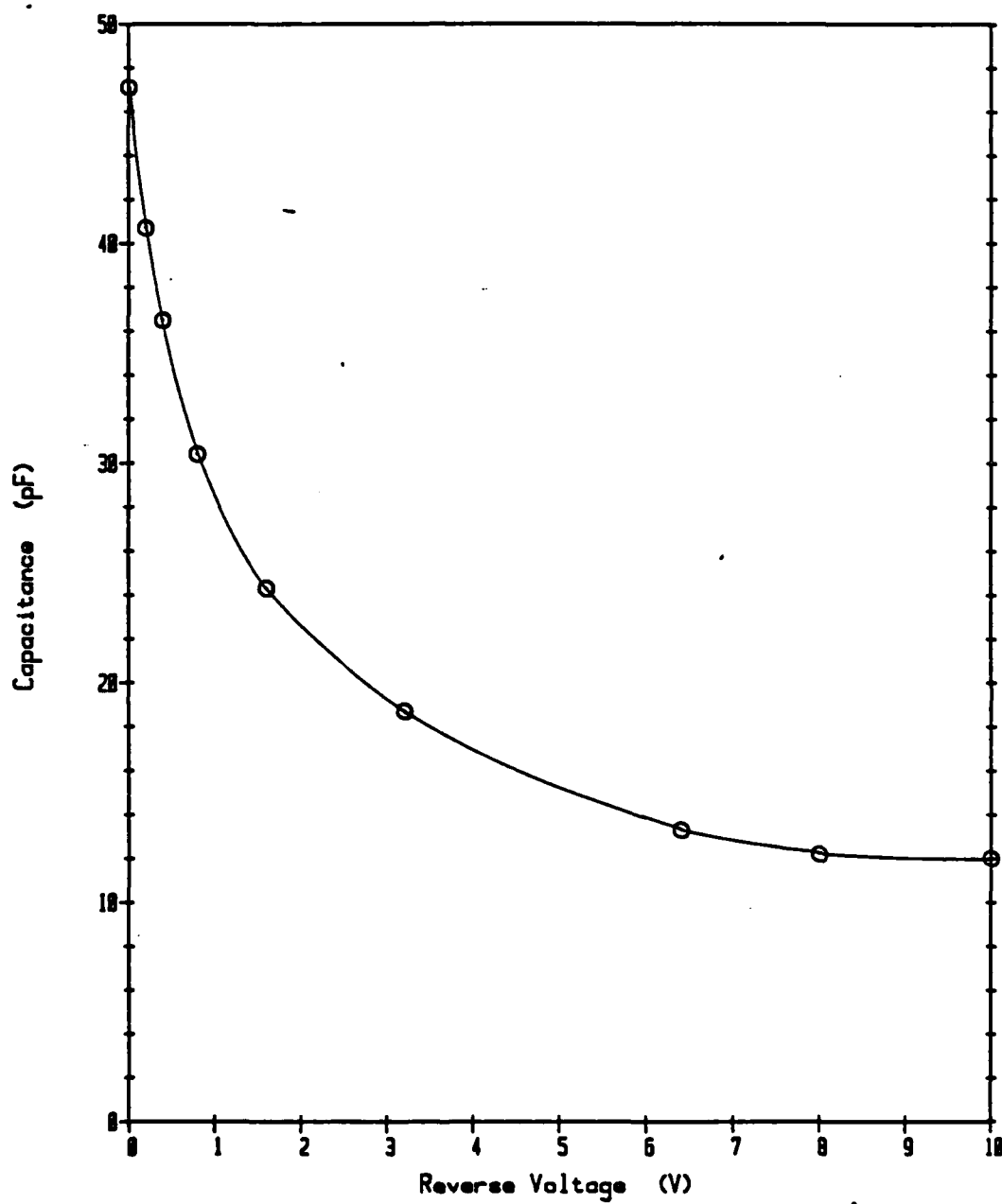


Figure 4.1 Sample 2A26 capacitance analysis.

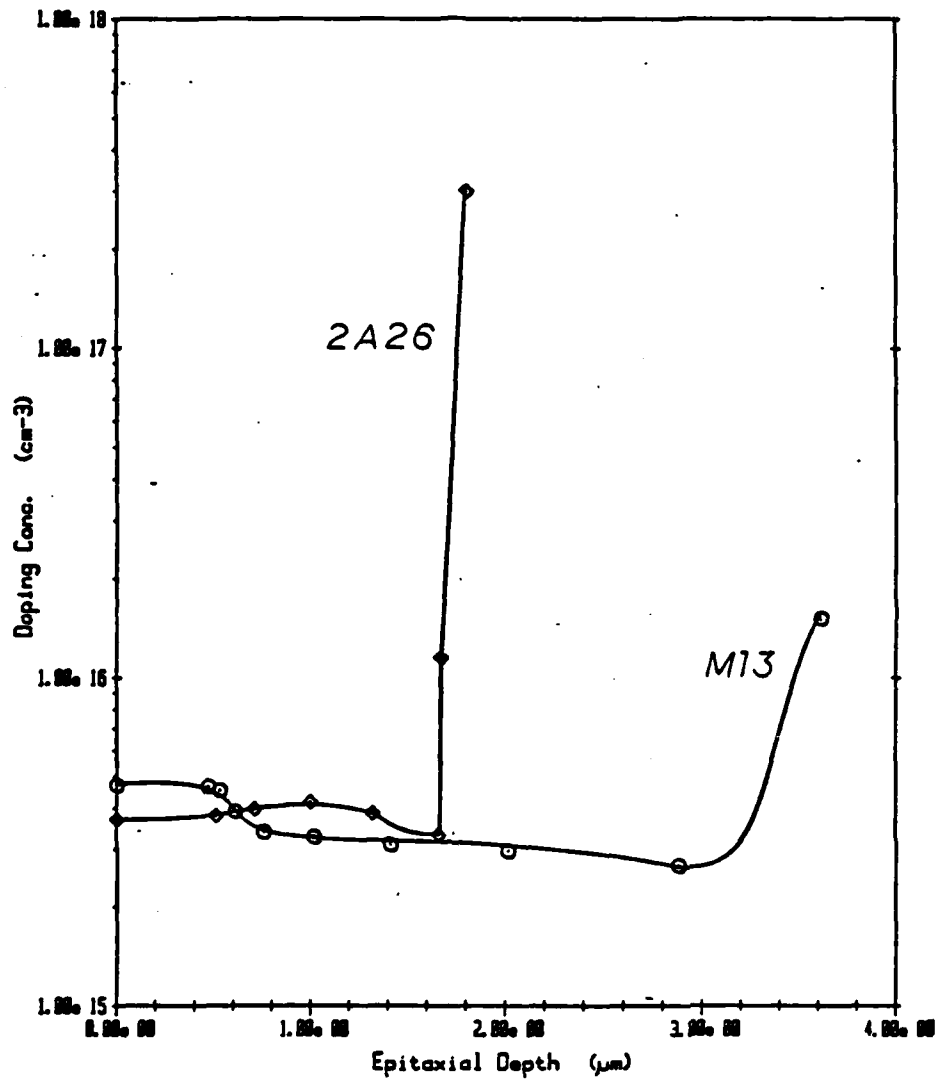


Figure 4.2 Samples 2A26 and M13 doping profiles.

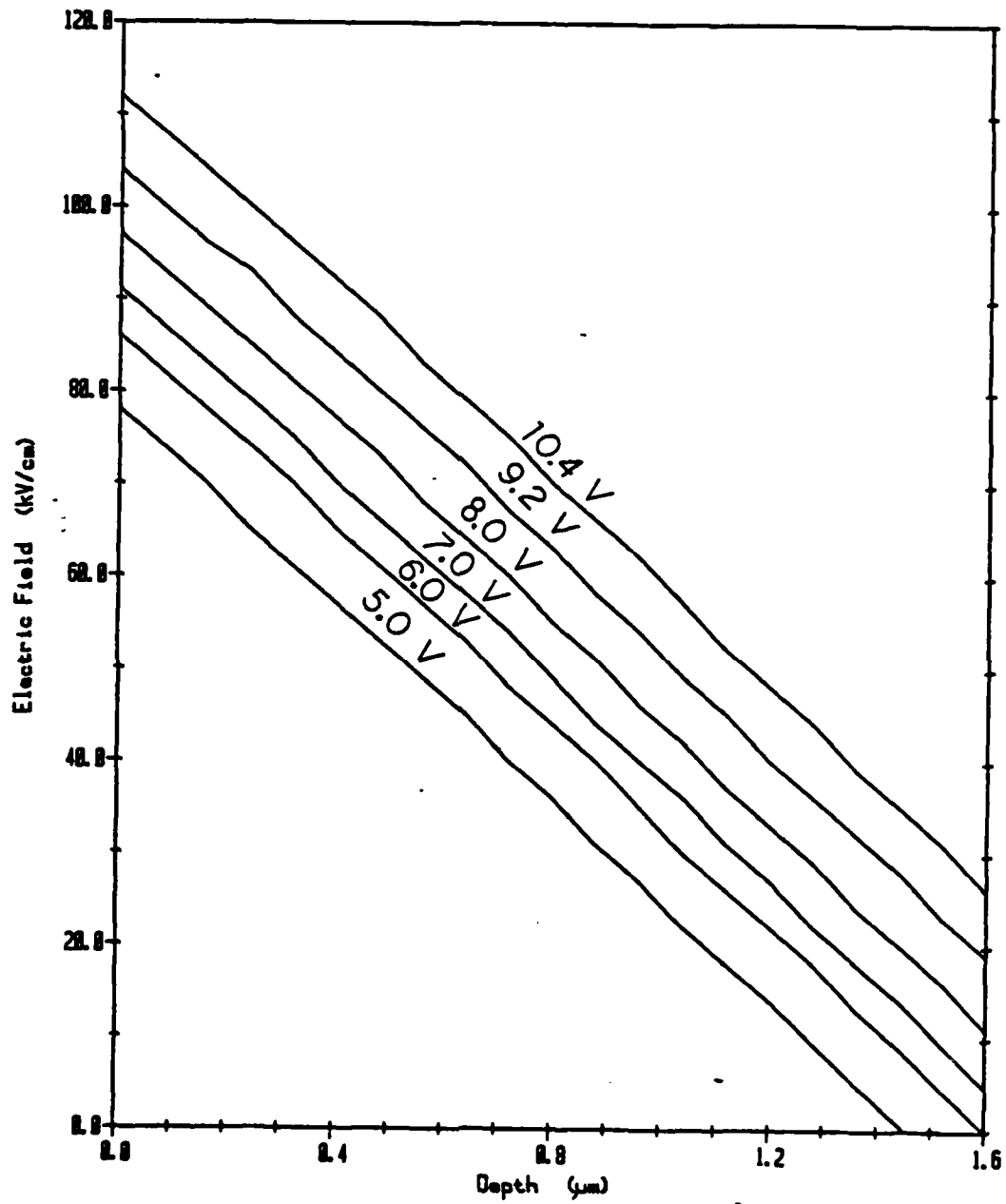


Figure 4.3 Sample 2A26 electric field profile with reverse bias.



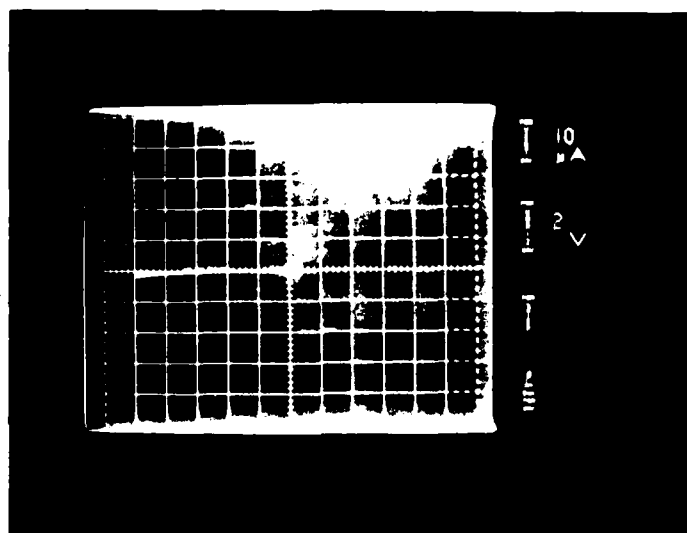


Figure 4.4 Sample 2A26 current-voltage relationship.

evaporated aluminum. Most samples appeared as open circuits. Other fabrication difficulties produced rather poor Schottky contacts so only two out of ten samples made were usable. The I-V curve in Figure 4.4 was measured on the 2A26 #2 sample which was used in these measurements. The limit of reverse bias for this sample was 11 volts as leakage currents were too large at higher biases.

The sample was placed in the measurement circuit depicted in Figure 3.17. Phase vs. voltage data was taken at 300 K with a beam potential of 6.85 kV. Table 4.1 shows the measured phases along with their applied voltages. To establish a starting point for analysis, Evans and Robson's (3) data was integrated using equation (2.18) on the electric field interval of the first applied bias. The phase which was generated was taken as that of the first measurement. All the other phases were offset by a constant equal to the difference between the measured first phase and the generated first phase. Table 4.1 also shows the adjusted phases which were entered into the numerical analysis program along with the applied voltages and the sample doping profile. This adjustment was necessary to speed up the numerical analysis and should have no effect on the  $v(E)$  curve if extrapolation to zero velocity for zero electric field is assumed.

This phase-voltage data along with the doping profile were entered into the Newton-Raphson numerical analysis program on the HP 9825S desk top calculator which augmented the initial  $v(E)$  guess to fit the measured data. Figure 4.5 shows the curve generated by the program. The flat region from 26 kV/cm to 80 kV/cm is a result of a

Table 4.1 Measured and adjusted phase vs. applied voltage for the 2A26 #2 sample.

<u>V</u>	<u><math>\phi</math>adjusted</u>	<u><math>\phi</math>measured</u>
-5.0	-0.5480	0.5190
-5.2	-0.5625	0.5045
-5.4	-0.5682	0.4988
-5.6	-0.5970	0.4700
-5.8	-0.6015	0.4655
-6.0	-0.6045	0.4626
-6.2	-0.6052	0.4618
-6.4	-0.6062	0.4608
-6.6	-0.6084	0.4586
-6.8	-0.6105	0.4565
-7.0	-0.6117	0.4553
-7.2	-0.6111	0.4553
-7.4	-0.6121	0.4549
-7.6	-0.6161	0.4509
-7.8	-0.6188	0.4482
-8.0	-0.6206	0.4464
-8.2	-0.6230	0.4440
-8.4	-0.6253	0.4417
-8.6	-0.6275	0.4395
-8.8	-0.6296	0.4374
-9.0	-0.6320	0.4350
-9.2	-0.6352	0.4318
-9.4	-0.6370	0.4300
-9.6	-0.6392	0.4278
-9.8	-0.6417	0.4253
-10.0	-0.6450	0.4220
-10.2	-0.6484	0.4186
-10.4	-0.6484	0.4186

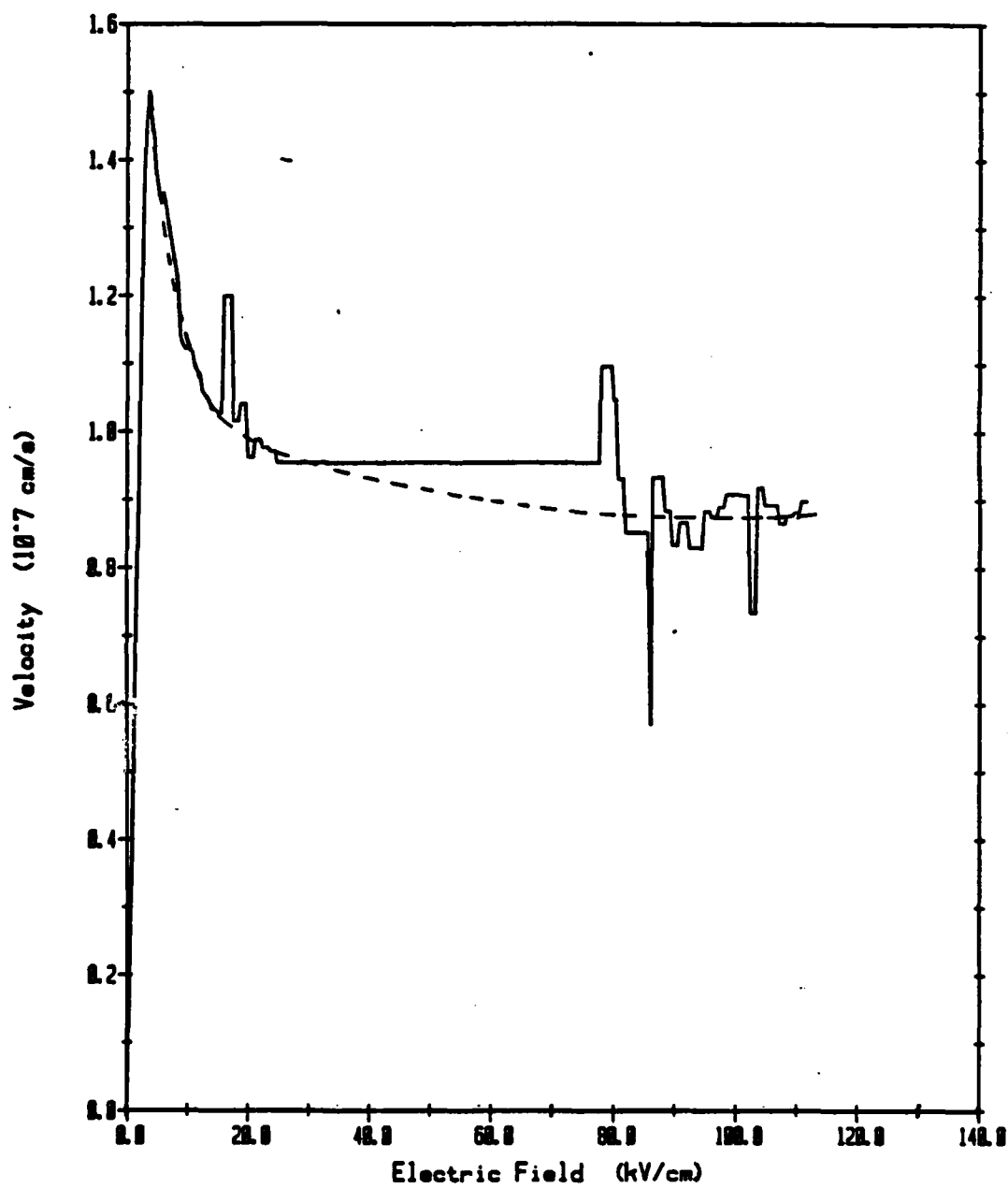


Figure 4.5 Measured  $v(E)$  curve for sample 2A26.

lack of resolution in the measurements in this area. In Figure 4.3 the electric field profile for the highest voltage, 10.4 V, and the smallest, 5.0 V, applied reverse bias are shown. The lowest electric field value for 10.4 V is 26 kV/cm and the highest field intensity for 5.0 V is 78 kV/cm. This area of the  $v(E)$  curve is common to all the measurements and changes made in its shape will have little effect on the difference between generated phases. The curve in this area can only be offset up or down but its shape cannot be determined for normal doping profiles. Reverse bias measurements were not made below 5.0 V because of varying bond area capacitance and short depletion lengths. Noise in the circuit prevented examination of depletion lengths less than 1.5 microns because the induced phase shift is too small.

The large discontinuities in the  $v(E)$  plot at certain points are probably due to compensation for the flat section of the curve in the numerical analysis. If a smooth line is drawn through the average of the plot, a more reasonable estimate of the curve's shape can be made. The curve seems to exhibit an asymptotic decrease at high fields suggesting that there is a saturation velocity.

The amount of error in the high field section of the curve may be as much as ten percent. Phase variation with the small change in velocity in this region is difficult to determine. This phase uncertainty along with the resolution of the ANA (about 3 degrees) weakens faith in this data. Longer samples would be useful to better the phase resolution for small changes in velocity.

An expansion of the low field region (0 to 12 kV/cm) of the  $v(E)$  curve is shown in Figure 4.6. The resolution is better in this area although numerical jumps in the curve are still evident. The peak velocity is  $1.5 \times 10^7$  cm/s at 3.6 kV/cm and the numerical deviations were less drastic. The negative differential mobility is measured to be about  $400 \text{ cm}^2/\text{Vs}$  at 7.5 kV/cm.

Finer electric field increments could have been made, however, limits on the measurement system's resolution and on the number of measurements the calculator could analyze made this prohibitive.

#### 4.2 ANALYSIS OF WINDHORN'S DATA

Phase vs. applied voltage measurements were performed by Thomas H. Windhorn at the University of Illinois (4,5). With his cooperation his phase-voltage and doping profile data were analyzed using the Newton-Raphson iterative technique described earlier. Figure 4.7 shows the electric field profiles for his samples at the reverse bias values shown. Table 4.2 presents the measured phase with respect to applied voltage. The phases were adjusted as described in section 4.1 to speed up the numerical analysis. The adjusted phases in Table 4.2 along with the applied voltages and the doping profile were entered into the numerical analysis program and the result was the curve in Figure 4.8. Again, numerical deviations are evident. However, the field variation across the sample is

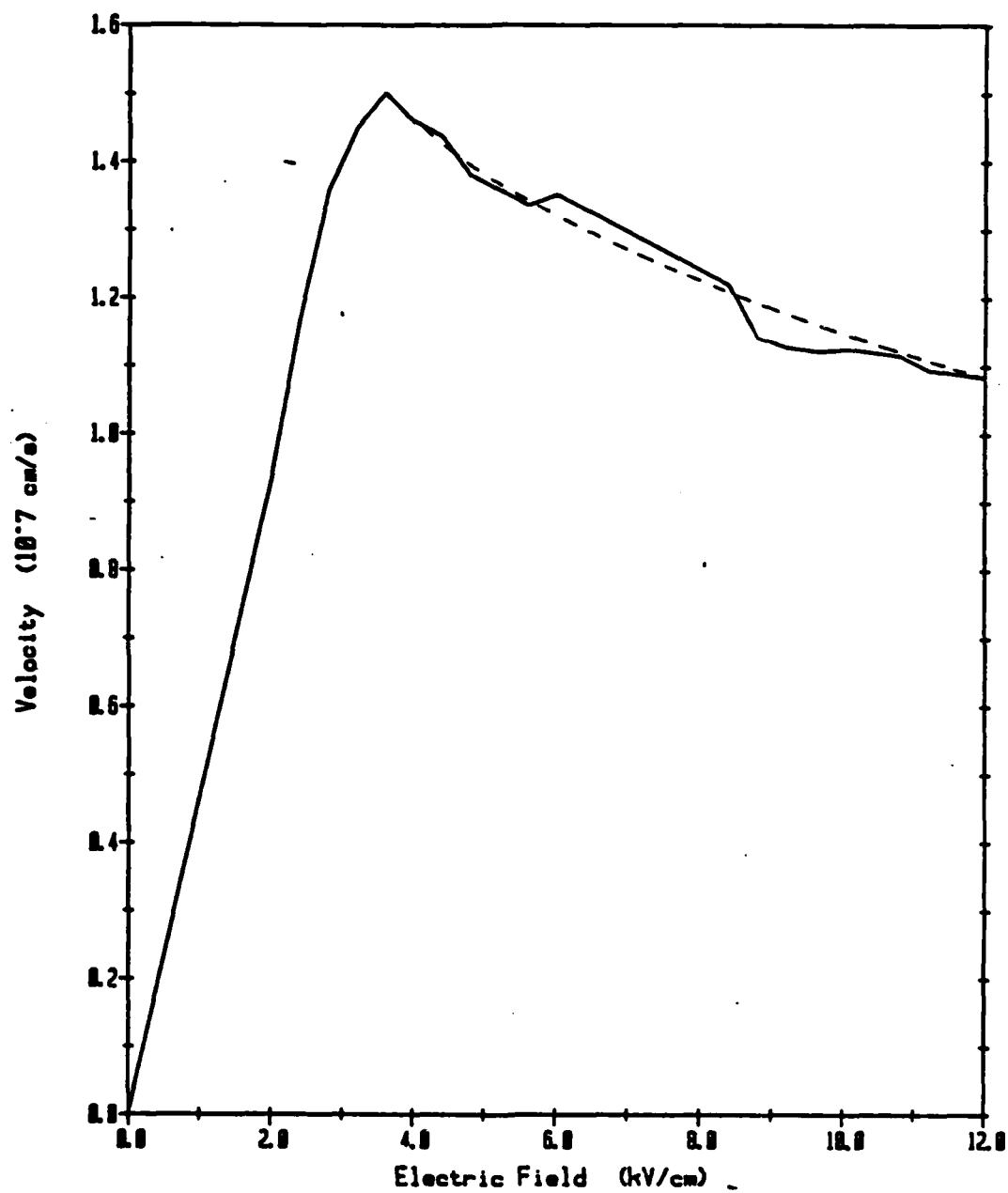


Figure 4.6 Low field velocity curve.  
Close up of Figure 4.5.

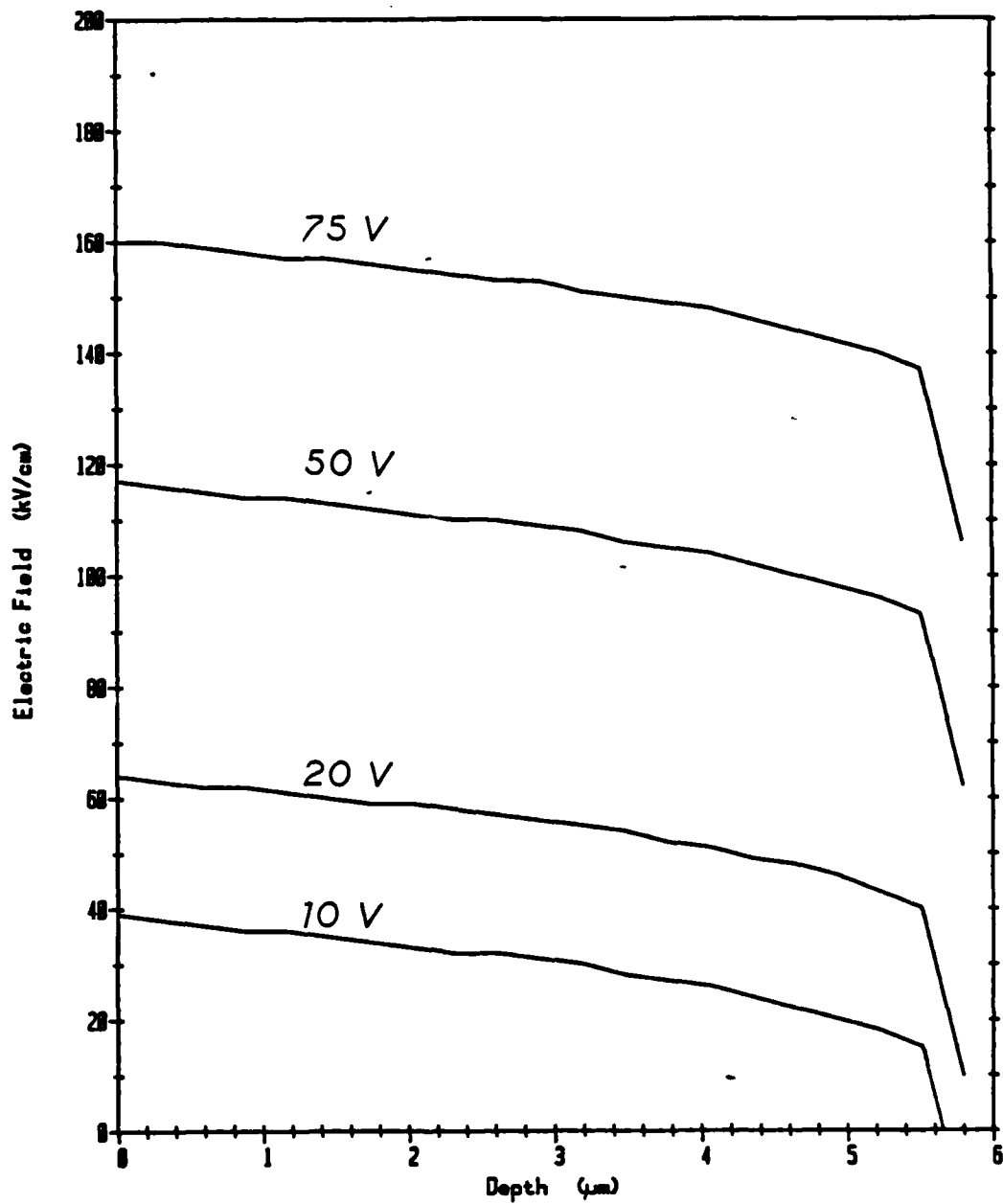


Figure 4.7 Electric field profile with reverse bias for T. Windhorn's samples.



Table 4.2 Adjusted phase vs. applied voltage  
from T. Windhorn's measurements.

<u>V</u>	<u><math>\phi</math>adjusted</u>	<u><math>\phi</math>measured</u>
-1.0	- .713	.593
-2.0	- .826	.480
-3.0	- .939	.367
-4.0	-1.044	.262
-5.0	-1.114	.192
-6.0	-1.184	.122
-7.0	-1.227	.079
-8.0	-1.262	.044
-9.0	-1.219	.017
-10.0	-1.306	-.00001
-15.0	-1.393	-.087
-20.0	-1.463	-.157
-25.0	-1.511	-.205
-30.0	-1.559	-.253
-35.0	-1.598	-.202
-40.0	-1.646	-.340
-45.0	-1.699	-.393

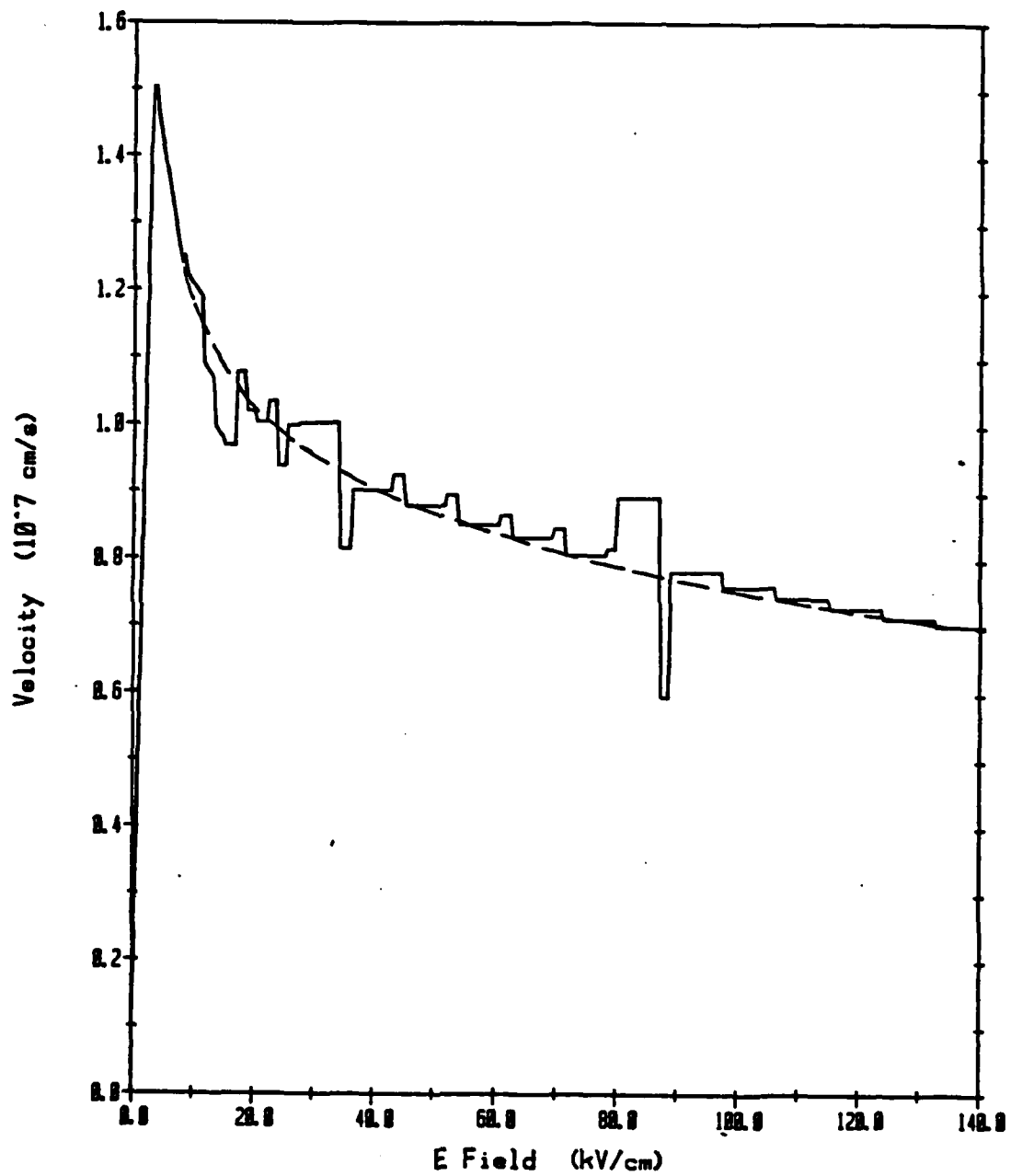


Figure 4.8 Calculated  $v(E)$  curve from Windhorn's phase-voltage data.

small enough (20 kV/cm) and the Schottky was very good so high reverse biasing could be achieved. Therefore, electric field limits were calculated across the entire area of numerical analysis. No large flat region is observed and an average line is in closer proximity with the actual curve. The smooth curve agrees with Dr. Windhorn's published results exactly.

#### 4.3 COMPARISON OF OUR RESULTS WITH WINDHORN'S RESULTS

The purpose of T. Windhorn's data was to measure the high field region of the  $v(E)$  curve. These measurements are too coarse to be used for examination of the curve at or about the peak velocity point. Comparisons should, therefore, only be made with other data at high fields ( $>10$  kV/cm).

Figure 4.9 is an overlay of the  $v(E)$  curve as generated from Windhorn's phase-voltage data and that which satisfies our data. At electric field values within 20 kV/cm of the peak the curves track within less than 10 percent of each other. At higher fields ( $>50$  kV/cm) Windhorn's data indicates a constantly decreasing velocity with electric field. Our curve begins to flatten and approaches a constant velocity of about  $8.8 \times 10^6$  cm/s above 80 kV/cm. This is a major discrepancy as to the value of the second valley mobility and where it may become noticeable. Further experimentation is

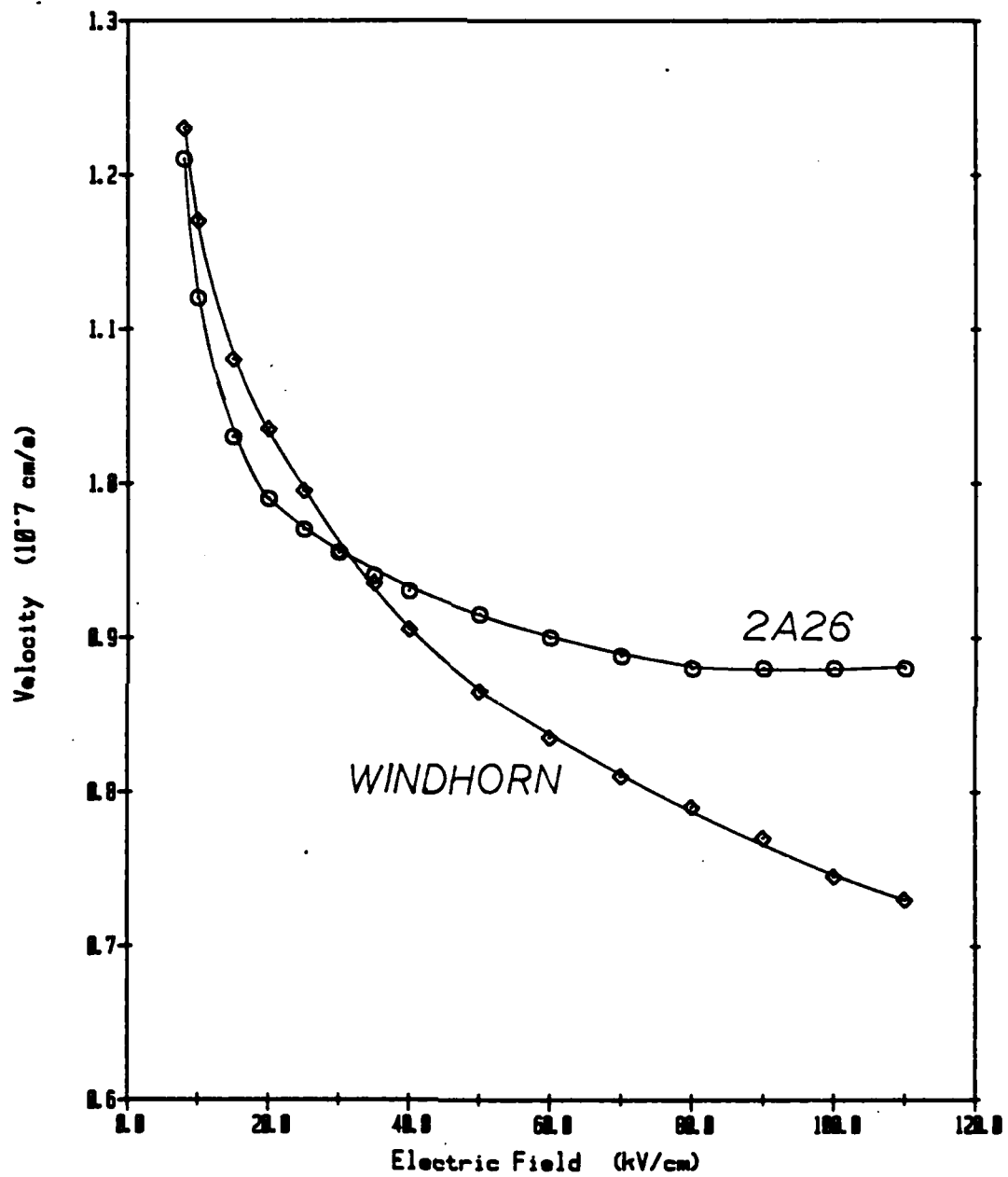


Figure 4.9 Comparison of calculated  $v(E)$  curves.

required to understand this difference in the results or to prove which relationship is correct.

## 5. CONCLUSIONS

### 5.1 LIMITATIONS OF THE UNIFORM FIELD APPROXIMATION

Although it has been shown that this is not the case for the samples used in these experiments, a velocity-field relationship can be derived from the phase-voltage data in Table 4.1 using the uniform field approximation. The electric field is taken as the applied bias voltage divided by the epitaxial layer length and the velocity is calculated using equation 1.6. Figure 5.1 shows the resulting uniform field curve and the curve generated using a non-uniform field numerical method.

The electric field variation across the depletion region in the punched-through case for our sample was about 90 kV/cm. The uniform field approximation tends to compress the range of measurement in the electric field and arrive at an average velocity for the interval of the  $v(E)$  curve being sampled in the measurement point. In comparison the uniform curve demonstrates a higher velocity compared to the same interval on the non-uniform curve. This demonstrates the increased accuracy of the non-uniform field numerical method over the simplified uniform field approximation.

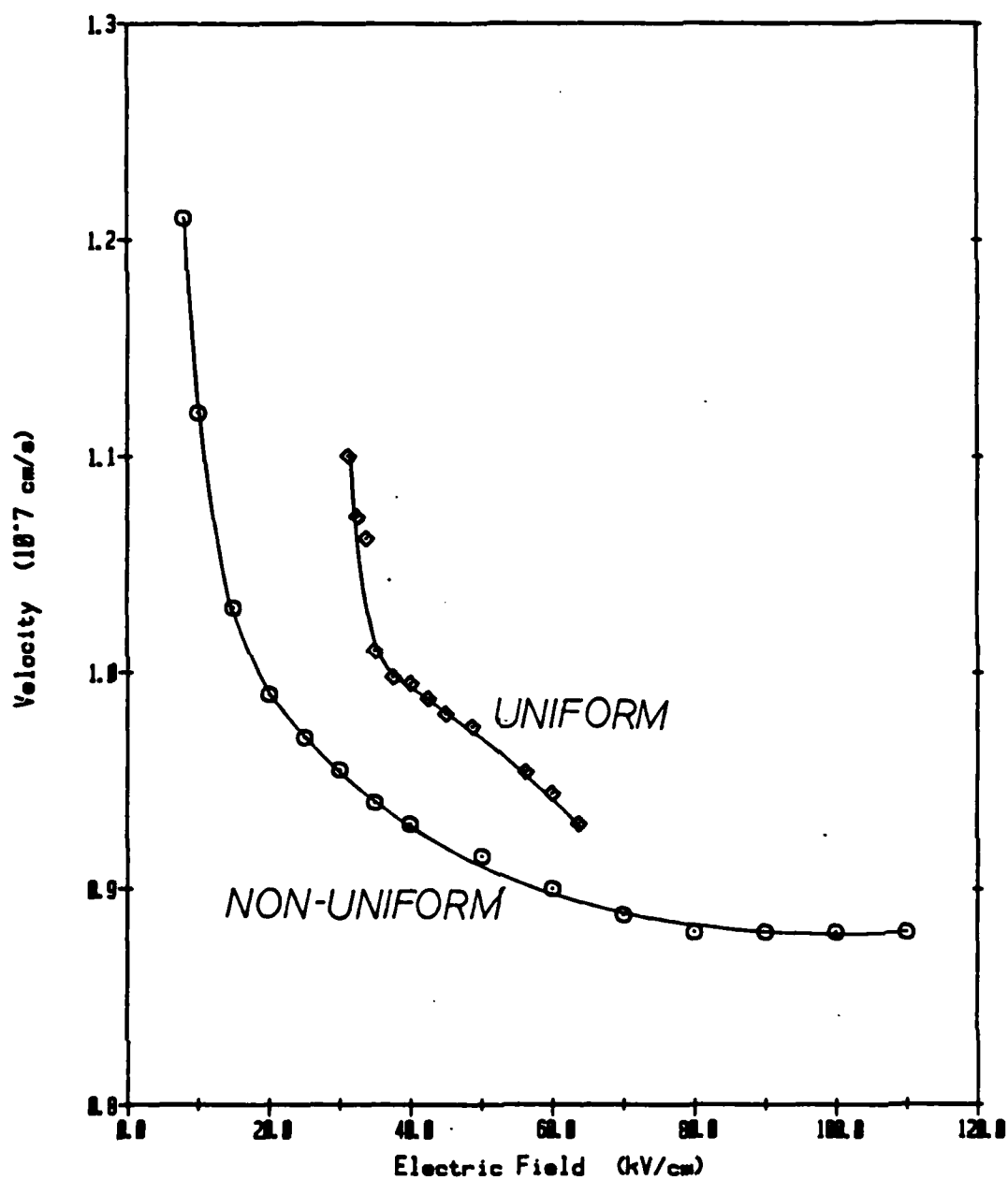


Figure 5.1 Comparison of non-uniform field solution with uniform field solution.

## 5.2 SUMMARY

To measure the velocity of electrons drifting through a semiconductor material relative to the internal electric field, a microwave frequency modulated electron beam injection system was built and demonstrated. In order to permit the examination of samples with high doping concentrations ( $>10^{15} \text{ cm}^{-3}$ ), the effect of a non-uniform electric field taper was accounted for in the analysis of the measured signal phase-voltage data. The numerical techniques employed required shorter samples than those usually used in previous  $v(E)$  measurements. For adequate phase resolution high carrier injection rates were necessary (12 GHz).

An electron gun and reliable high voltage supply were assembled to provide a 330 nA beam. An efficient 6 GHz modulator was designed and employed, giving good single frequency, single mode transverse beam modulation. RF power was transmitted through the glass vacuum envelope so the vacuum was not compromised. Amplification of the low power 12 GHz test signal was necessary to measure the injected sample current phase-reverse applied voltage relationship.

An examination of the sample package parasitics was performed to determine non-punched-through phase behavior. The voltage dependence of the bond pad area capacitance ( $C_p$ ) and the size of the bond-wire inductance were discovered to be non-negligable. Calibration with an open package would not take these impedances into account and would therefore be useless. A zero velocity was



assumed for a zero applied electric field so a reference was established for the  $v(E)$  curve.

Implementation of this scheme yielded a good estimation of the  $v(E)$  curve around the peak. This data correlates well with other low field measurements. Numerical analysis of T. Windhorn's (4,5) data has demonstrated good agreement with the uniform field approximation for lightly doped material at high electric fields. The electric field variation across the sample length was small ( $<20$  kV/cm) so for areas on the  $v(E)$  curve of small velocity variation with electric field the approximation is appropriate.

Good samples were not available in quantity before the end of this project. Truly conclusive data, therefore, could not be obtained about the high field nature of the generated  $v(E)$  curve. Further experimentation is needed to establish the behavior of the drift mobility for high fields.

Examination of the electric field profiles of higher doped semiconductor samples has led to the design of samples to improve the range and accuracy of measuring the  $v(E)$  relationship using the numerical analysis method presented here. To get high enough resolution for close examination of the peak of the  $v(E)$  curve, lightly doped (about  $2 \times 10^{14} \text{ cm}^{-3}$ ) material is necessary to decrease the electric field taper. Epitaxial layer lengths of about  $5 \mu\text{m}$  would provide a field taper of about 10 kV/cm to permit detailed estimation of the low field influence on electron velocity. Smaller bond pad areas will help decrease the influence of parasitic capacitance variation on the phase. Experience in making these

measurements has led to a few specific suggestions to improve the technique for higher doped material.

### 5.3 RECOMMENDATIONS

A more lightly doped sample (about  $7 \times 10^{14} \text{ cm}^{-3}$ ) with a longer epitaxial layer (about 4 microns) would allow enough field variation to examine the  $v(E)$  curve up to about 200 kV/cm. The longer sample lengths would also allow larger phase shifts for smaller electric field increments increasing the resolution of the resulting curve. Very good Schottky contacts are also necessary for high reverse biases to improve the range of measurement.

Numerical analysis should be executed on a more powerful computer than the HP 9825. Ideally an intelligent choice of bias points can minimize the number of measurements by increasing the resolution around regions of high mobility variation with electric field (i.e. the knee of the curve for III-V materials) and having lower resolution in areas of less velocity variation. Even with this selective method of examination, the number of measurements required to analyze a large part of the curve would be about 200. With specialized numerical analysis techniques and advanced program chaining methods the memory requirements and sheer computing power necessitates the use of a minicomputer if not a main frame.

Diffusion characteristics for semiconductors is also important in the understanding of device behavior. To measure its dependence a means of varying the charge pulse width and separation within the depletion region would be ideal. A modulator with a large frequency range, say 6 to 8 GHz, would be useful to vary the pulse injection rate. The variation in charge separation along with knowledge of the  $v(E)$  curve should yield enough information to estimate a diffusion-electric field relationship.

With these and other appropriate improvements the CW time-of-flight measurement technique should be applicable to a variety of measurements on any semiconductor material on which a non-conducting contact can be made and an internal electric field can be established.

## 6. ACKNOWLEDGEMENTS

The author would like to thank Dr. Robert Goldwasser for insight into the electronics of the experiment, design suggestions and supplying adequate GaAs material for measurement.

Recognition also goes to David Walker and Jerome Teng for fabrication of the samples used in the measurement.

Thanks also goes to Rick Kiehne of Central Microwave Corporation for his help in assembly of the detection and amplification circuitry.

7. APPENDICES

APPENDIX 1  
Computer Programs

```

0: "11863C SOFTWARE FOR SYSTEM FOR TRANSPORT";
1: "ANALYSIS OF SEMICONDUCTORS, 4/8/82";
2: "P/N 11863-10003, WASHINGTON UNIVERSITY MICROWAVE LAB";
3: "MODIFIED BY GLEN HOMSEY ON DISK UNDER NewTas";
4:
5: dsp "TAS MEASUREMENT PROGRAM";wait 2000
6:
7: "TEST CONDITIONS SECTION";
8: "INITIALIZATION";
9:
10: ent "Enter the number of meas. pts.",N
11: dim X[N],Y[N],E[2],U[N],Z[N]
12: dim A[6],B[6],D[N],K[2],O[3],Q[N],T[3],V[N]
13: dim E0[7],P0[4],S0[20]
14:
15: dev "A",710,"S",706,"R",716,"W",714,"G",704,"P",713
16:
17: "CAPACITANCE OF OPEN",.001)K[1]
18:
19: "SYSTEM IMPEDANCE",50)K[2]
20:
21: rad;cli 7;icl 7;rem 7
22:
23: "CALIBRATION SECTION";
24:
25: beep;cfg 5;dsp "SET TEST CHANNEL GAIN TO 60 dB";stp
26: "STORE BEAM CENTER OFFSETS";
27: beep;dsp "HOLD BEAM CTR and PRESS CONTINUE";stp
28: 1)Q)Z;gsb "Aver"
29: V)O[1];2)Z;gsb "Aver"
30: V)O[2]
31: beep;dsp "Place 10V Rev. Bias on Diode";stp
32: 1)Q;gsb "Atten"
33: cfg 7;1)I;gsb "Read"
34: Dmtn*(.5(6-Q))/8)O[3];sfg 7
35: 0)0
36: 1)E[1];0)E[2];gto "Meas"
37: ent "Is Calib. Data on Tape? (Y/N)",P0
38: if cap(P0[1])="Y";gto "Caload"
39:
40: "S21cal";
41: gsb "Thru"
42: ent "Want To Store Calib. Data? (Y/N)",P0
43: if cap(P0[1])="Y";gto "Calstor"
44:
45: "MEASUREMENT SECTION";
46:
47: "Meas";
48: 1)C;1)G;beep;ent "Enter Sample Length (um)",H
49: H*1e-6)H
50: beep;dsp "Set Up Device Under Test";stp
51: ent "Enter Modulation Freq (MHz)",F
52: "MeasAgN";
53: sfg 5
54: beep;ent "Enter Bias [Volts]",V[C]
55: F)Z[C]
56: 8)I
57: gsb "Loop"
58: cli "Rtop"(X[C],Y[C],D[C],Q[C])
59: if C=N;gto "Table"

```

```

60: C+1)C;gto "MessAgn"
61:
62: "MAIN MEASUREMENT LOOP"=====,
63:
64: "Loop":
65: gsb "Read"
66: if I=8;gsb "Normal"
67: ret
68:
69: "CHECK DATA SECTION"=====,
70:
71: "Check":
72:
73: cll "Rtop"(XIC),YIC,DIC,QIC)
74: -(M2e6MMZIC)/QIC)UIC,fit 3
75: dsp "VELOCITY =",UIC,"m/sec";beep;stp
76: ent "Want to retake this pt? (Y/N)",P$
77: if cap(P$(1))="Y";gto "MessAgn"
78: if C=N;gto "Table"
79: ent "Continue to next pt? (Y/N)",P$
80: if cap(P$(1))="Y";C+1)C;gto "MessAgn"
81: dsp "WAITING";stp
82: C+1)C;gto "MessAgn"
83:
84: "DATA OUTPUT SECTION"=====,
85:
86: "Table":
87: ent "Enter Table Title (<20 Char.)",S$
88: fmt 1,c,2;/wrt "M.1",S$
89: fmt 1,"DATA PT",z;wrt "M.1"
90: fmt 2,8x,"PHASE (rad)",z;wrt "M.2"
91: fmt 3,4x,"MAGNITUDE",z;wrt "M.3"
92: fmt 4,6x,"FREQ (MHz)",z;wrt "M.4"
93: fmt 5,6x,"BIAS (V)",z;wrt "M.5"
94: fmt 6,7x,"LENGTH (um);wrt "M.6"
95: for C=1 to N by 1
96: fmt 1,3x,f2.0,z;wrt "M.1",C
97: fmt 2,10x,f6.4,z;wrt "M.2",QIC
98: fmt 3,10x,f5.3,z;wrt "M.3",DIC
99: fmt 4,10x,f5.0,z;wrt "M.4",ZIC
100: fmt 5,10x,f7.3,z;wrt "M.5",VIC
101: fmt 6,9x,f9.2;wrt "M.6",MM1e6
102: next C
103:
104: dsp "DONE";stp
105:
106: "SUBROUTINES SECTION"=====,
107: "Caload":
108: beep;dsp "Insert Data Tape";wait 2000
109: ent "Enter Track to Find Calib. Data",I
110: ent "Enter File to Find Calib. Data",J
111: trt I,ldf J,E(M)
112: gto "Mess"
113:
114: "Calstor":
115: beep;dsp "Insert Data Tape";wait 2000
116: ent "Enter Track To Store Calib. Data",I
117: ent "Enter File To Store Calib. Data",J
118: trt I,ref J,E(M)
119: gto "Mess"
120:
121: "Read":
122: "Ch1",1)Z;gsb "Aver"

```



```

123: V=0[1]E
124: "Ch2":2)Z,gsb "Aver"
125: cll "Rtop"(E,V=0[2],B,A)
126: if B>2.2,gto "Up"
127: if B<.4,gto "Down"
128: "Ch3":if Q<3 and flg7,0[3]B/tn^(.5(6-Q))D,gto +3
129: 4)Z,gsb "Aver"
130: tn^(V-.5(6-Q))D
131: cll "Ptor"(D,A,X,Y)
132: if flg5,gto "Data"
133: "Cal":X)E[1],Y)E[2],ret
134: "Data":X)X[C],Y)Y[C],ret
135: "Up":
136: Q+1)Q;if Q>6,6)Q,prt "OVERRANGE",gto "Ch3"
137: gsb "Atten"
138: gto "Read"
139: "Down":
140: Q-1)Q;if Q<1,1)Q,gto "Ch3"
141: gsb "Atten"
142: gto "Read"
143:
144: "AVERAGE MEASUREMENTS":
145:
146: "Aver":
147: 0)U,500)D
148: for L=1 to D
149: gsb "Volt"
150: U+V)U
151: next L
152: (U/D).0025)V
153: ret
154:
155: "59313A A/D READING":
156:
157: "Volt":
158: fnt 1,"H",f.0,"AJ",wrt "A.1",Z
159: ret(rdb("A"),8)+rdb("A"))V
160: ret
161:
162: "SET 8418 IF ATTENUATION":
163:
164: "Atten":
165: fxd 0
166: beep,dsp "SET TEST CHANNEL GAIN TO",10(7-Q),stp
167: ret
168:
169: "CALIBRATION WITH THRU-SINGLE PATH":
170:
171: "Thru":
172: if 0#1,beep,dsp "Conn Calib Section",stp
173: 1)1,1)0,sfg 10,gsb "Loop"
174: cfg 10
175: ret
176:
177: "MATH DURING MEASUREMENT":
178:
179: "Normal":
180: cll "Cd1v"(X[C],Y[C],E[1],E[2],T[2],T[3])
181: T[2])X[C],T[3])Y[C]
182: ret
183:
184: "POLAR TO RECTANGULAR":
185:

```

```

186: "Ptor",
187: p1cos(p2)}p3
188: p1sin(p2)}p4
189: ret
190:
191: "RECTANGULAR TO POLAR",
192:
193: "Rtop",
194: \((p1p1+p2p2)}p3;sfg 14
195: 2*tn(p2/(p1+p3))}p4
196: csg 14;ret
197:
198: "COMPLEX DIVIDE",
199:
200: "Cdiv",
201: p3p3+p4p4}p7
202: (p1p3+p2p4)/p7}p5
203: (p2p3-p1p4)/p7}p6
204: ret
205:
206: end
≡12600

```

AD-A121 734

SYSTEM TO MEASURE CARRIER DRIFT VELOCITY IN  
SEMICONDUCTOR MATERIALS(U) WASHINGTON UNIV ST LOUIS MO  
DEPT C ELECTRICAL ENGINEERING G N HOMSEY ET AL.

272

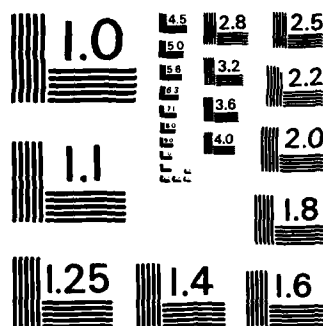
UNCLASSIFIED

AUG 82 82-4-DNR N00014-79-C-0840

F/G 20/12

NL





MICROCOPY RESOLUTION TEST CHART  
NATIONAL BUREAU OF STANDARDS-1963-A

```

0: 'v(E) Numerical Analysis Program for Arbitrary Q(V)';
1: 'Developed by Glen Homsey, 7/8/82, On Disk Under CorRef';
2:
3: rad
4:
5: dsp 'v(E) NumAnl Prog for Any Q(V)';wait 2000
6: ent 'Enter Modulation Freq. in Hz',M
7: flt 3;prt 'Mod Freq=',M;MM2M{}M
8: ent 'Enter Number of Meas. Pts.',N
9: ent 'Enter Number of Doping Pts.',M
10: ent 'Enter Epilayer Depth in microns',L
11: Lmie-6}L
12: ent 'Enter No. of Initial Guess Points',O
13: dim C{O},D{M},E{21,M},H{21},L{N},P{N},Q{N},S{O},V{O,N},X{M}
14: dim I{N},J{N,M},Y{M},U{O},F{O},G{O},O{O},W{O}
15: dim A{2,M},B{4,O}
16: 1.6021892e-19}Q;ent 'Enter Rel. Diel. Const.',r2
17: fxd 2;prt 'Rel Diel=',r2," "
18: Q/(r2/(36{}Lmie-9))Q
19:
20: beep;dsp 'Doping Data Entry';wait 2000
21: dsp 'Enter X in microns and D in cm-3';wait 2000
22: prt 'Doping Data'," "
23: for I=1 to M
24: fxd 2
25: ent X{I};prt I,"X=",X{I}
26: flt 3
27: ent D{I};prt "D=",D{I}," "
28: X{I}mie-6}X{I};D{I}mie6}D{I}
29: next I
30: prt " "
31: fxd 2;0}F{1}
32: for I=1 to M-1
33: cll 'CorrTrap'(1,X{I},X{I+1},X{I+2},D{I},D{I+1},D{I+2},A)
34: A=F{I}F{I+1}
35: next I
36: .5{}D{M}+D{M-1}){}X{M}-X{M-1})+F{M-1})F{M}
37: for I=1 to M-1
38: cll 'PeeLin'(X{I},X{I+1},F{I},F{I+1},A{1,I},A{2,I})
39: next I
40: 0}Y
41: for K=1 to 21
42: Y=L/20}Y
43: for I=1 to M-1
44: if X{I}<Y and Y<X{I+1}+1e-9,D{I}*(-1)}H{K},M-1}I
45: next I
46: next K
47:
48: beep;dsp 'Phase vs. Voltage Entry';wait 2000
49: dsp 'Enter Phase in radians';wait 2000
50: prt 'Phase','Information'," "
51: for I=1 to M
52: ent Q{I};prt I,"Q=",Q{I}
53: ent V{I};prt "V=",V{I}," "
54: V{I}-.75}V{I}
55: next I
56: prt " "
57: 1}{}J,0}X{V{O}}A}U,cfg 1
58: 'Step';
59: X=L/500}X

```

```

60: if X>L, goto "Punch"
61: "Step":
62: if X(J+1)<X(J+1)J,V+V(I-1)U,sfg 1, goto "Step"
63: -X(A(I,J)+A(2,J)X)F
64: if not flg1, jmp 2
65: (A(I,J)+A(2,J)X(X(J))/2)X(X(J))D
66: if flg1, jmp 2
67: (A(I,J)+A(2,J)X(A+X)/2)X(X-A)D
68: -V(I-1)D+U)V
69: if F+V(V(I),cfs 1,I+1)I,F/X)E(I,I-1),X)A,0)U,gsb "EGen"
70: if I=N+1, goto "Initial"
71: goto "Step"
72:
73: "Punch":
74: (V(I)-V)/L)E(I,I,I+1)I,gsb "EGen"
75: if I=N+1, goto "Punch"
76:
77: "Initial":
78: beep,ent "Enter Data File",J
79: trk 0,ldf J,U(M),F(M)
80:
81: for I=1 to M
82: call "Generate"(I)
83: L(I))I(I),fxd 4,prt P(I)
84: next I
85: prt " "
86: "Again":
87: for K=1 to M
88: call "Iterate"(K)
89: for J=1 to M
90: cfs 7
91: if E(21,J)<Z or V(E(I,J),0)J(J,K),sfg 7,next J
92: if flg7, goto 96
93: call "Generate"(J)
94: (L(J)-I(J))/1e3)J(J,K)
95: next J
96: call "Deiterate"(K)
97: next K
98: inv J)J
99: sapy -1M)I
100: mat JM)V
101: for I=1 to M
102: for S=1 to 0
103: if E(I,I)<F(S) and F(S)<E(21,I),Y(I)+U(S)U(S)
104: next S
105: next I
106: 1)X
107: for I=1 to M
108: call "Generate"(I)
109: 0)Y,if abs(L(I))<.001,1)Y
110: fxd 4,prt P(I)
111: XMY)X
112: L(I))I(I)
113: next I
114: prt " "
115: if X, goto "v(E) Plot"
116: goto "Again"
117:
118: "SUBROUTINES":
119:
120: "Generate":flt 3,cfs 8
121: E(1,p1)G(11,2)T
122: for S=0 to 1 by -1

```

```

123: if E[1,p1]<=F[S] and F[S]<=E[21,p1],U[S]^(-1))*W[T],F[S])G[T],sfg 8
124: if E[1,p1]<=F[S] and F[S]<=E[21,p1],T+1)*T,gab "Slope"
125: if flg8 and F[S]>E[21,p1],F[S])G[T+1],U[S]^(-1))*W[T+1]
126: if 1-S,jmp 2
127: if flg8 and F[S]>E[21,p1],F[S-1])G[T+2],U[S-1]^(-1))*W[T+2],cfg 8,1)*S
128: next S
129: W[21]*W[1],0[21]*0[1]
130: if flg8,T-1)*R)*T,G[T])G[T+1],W[T])*W[T+1],jmp 2
131: E[21,p1])G[T],(W[T-1]*W[T+1])/2)*W[T],0[T-1])0[T])0[T+1],T+1)*R
132: 0)*E,1)*C[1],0)*S[1]
133: for S=1 to R-1
134: call "CorrTrap"(p1,G[S],G[S+1],G[S+2],W[S],W[S+1],W[S+2],A)
135: AMO[S]=E
136: cos(NME)*C[S+1],sin(NME)*S[S+1]
137: next S
138: 0)*E)*F
139: for S=1 to R-1
140: call "CorrTrap"(p1,G[S],G[S+1],G[S+2],C[S],C[S+1],C[S+2],A)
141: AMO[S]=E
142: call "CorrTrap"(p1,G[S],G[S+1],G[S+2],S[S],S[S+1],S[S+2],B)
143: SMO[S]=F)*F
144: next S
145: \((F^2+E^2))*A,2*atan(-F/(E+A)))*P[p1]
146: (Q[p1]-P[p1])/Q[p1])*L[p1]
147: ret
148:
149: "PacLin":
150: (p4-p3)/(p2-p1))*p6
151: p3-p1*p6)*p5
152: ret
153:
154: "CorrTrap":
155: p3-p2)*r1,if r1=0,ret
156: (p6-p5)/r1)*r2,if p4-p3=0,r1/2*(p6+p5))*p8,ret
157: (p7-p6)/(p4-p3))*r3
158: r1/2*(p6+p5)+r1^2/12*(r2-r3))*p8
159: ret
160:
161: "Integrate":
162: p6*p2+p7*p2^2+p8*p2^3+p9*p2^4)*r1
163: p6*p3+p7*p3^2+p8*p3^3+p9*p3^4)*r2
164: r2-r1+p4)*p5
165: ret
166:
167: "EGen":
168: L/20)*Y,1)*r1,1-1)*r2,2)*r3
169: "Estep":
170: if X[r1+1]<Y,r1+1)*r1,gto "Estep"
171: E[1,r2]*A[1,r1]+A[2,r1]*W)*E[r3,r2]
172: if E[r3,r2]>0,0)*E[r3,r2],ret
173: if r3=21,ret
174: r3+1)*r3,Y+L/20)*Y,gto "Estep"
175:
176: "Iterate":
177: sfg 4
178: for I=1 to 0
179: cfg 5
180: if E[1,p1]<=F[I] and F[I]<=E[21,p1],U[I]+1e3)*U[I],F[I])*Z,sfg 5
181: if flg4 and flg5,F[I])*Y,cfg 4
182: if not flg4 and not flg5,0)*I
183: if E[1,p1]>F[I],0)*I
184: next I
185: ret

```

```

186:
187: "Deiterate":
188: sfg 4
189: for I=1 to 0
190: sfg 5
191: if E[1,p1]<=F[1] and F[1]<=E[21,p1],U[1]-1e3>U[1],cfg 4,cfg 5
192: if not flg4 and flg5,0]I
193: if E[1,p1]>F[1],0]I
194: next I
195: ret
196:
197: "Slope":
198: for U=20 to 1 by -1
199: if E[U,p1]<=F[S] and F[S]<=E[U+1,p1],H[U]0[I-1],1>U
200: next U
201: ret
202:
203: "v(E) Print":
204: flt 3
205: for I=1 to 0
206: if E[1,N]<=F[1] and E[21,1]>=F[1],prt "E",F[1],"V",U[1]," "
207: next I
208: gto "v(E) Dump"
209:
210: "v(E) Plot":
211: wrt 713,"pg1,in;ip1000,2000,7200,10000,"
212: -int(E[1,N]1e-6-1)10]2,1>Y
213: if Z>20,5>Y
214: if Z>50,10>Y
215: wrt 713,"ac0,"Z,"0,3,"
216: wrt 713,"xa0,"Y,"0,"2,"
217: fxd 0
218: for K=0 to Z by Y
219: wrt 713,"pa",str(K),"0,"
220: wtb 713,"cp0,-1,106,1b",str(K),3
221: next K
222: wrt 713,"pa",Z/2,"0,cp0,-3,"
223: wtb 713,"1bElectric Field in KV/cm",3
224: fxd 2
225: 3>A,if 0>1.371e9,5>A
226: wrt 713,"ya0,.25,0,"A,"
227: for K=0 to A by .25
228: wrt 713,"pa0,"str(K),"
229: wtb 713,"cp-3.5,0,108,1b",str(K),3
230: next K
231: fxd 6
232: wrt 713,"pa0,"A/2,"
233: wrt 713,"cp-10,0,d10,1,"
234: wtb 713,"1bVelocity x 10^7 cm/s",3
235: fxd 6
236: for I=1 to 0
237: if E[1,N]<=F[1] and E[21,1]>=F[1],gsb "Plot"
238: next I
239: gto "v(E) Dump"
240: "Plot":
241: if not flg10,wrt 713,"papu",-F[1]1e-5,"",U[1]1e-5,"",sfg 10
242: if flg10,wrt 713,"papd",-F[1]1e-5,"",U[1]1e-5,""
243: flt 3,prt U[1]
244: ret
245:
246: "v(E) Dump":
247: ent "Enter Track For v(E) Storage",J
248: ent "Enter File For v(E) Storage",K

```



```
249: trt J,ref K,U[M],F[M]
250: end
251:
252: "EDump":
253: for I=1 to N
254: fxd 2,prt V[I]
255: for J=1 to 21
256: flt 3,prt E[J,I]
257: if E[J,I]=0,21}J
258: next J
259: prt " "
260: next I
261: dsp "Dumped",stp
#17309
```

APPENDIX 2  
Machine Drawings

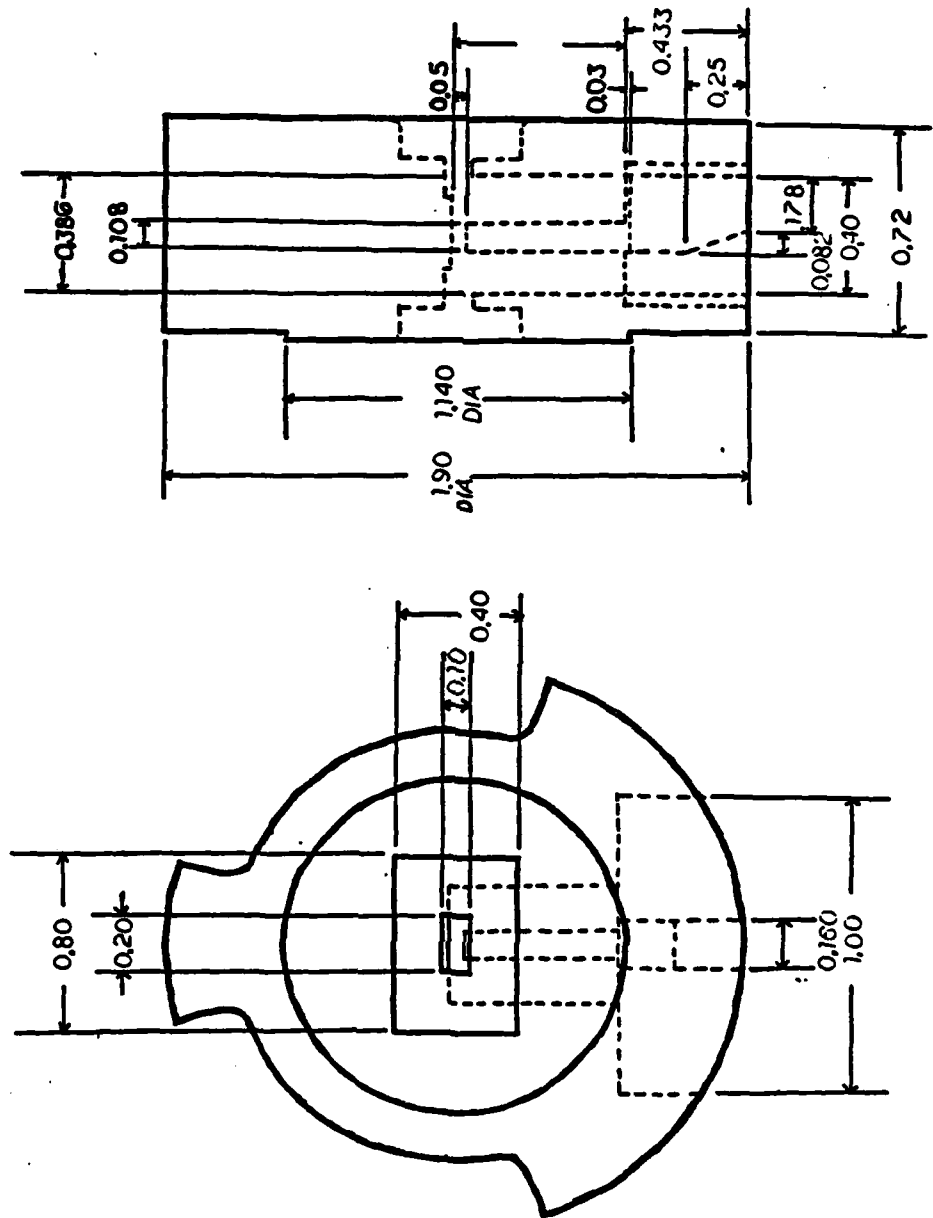


Figure A2.1 6GHz Modulator Body

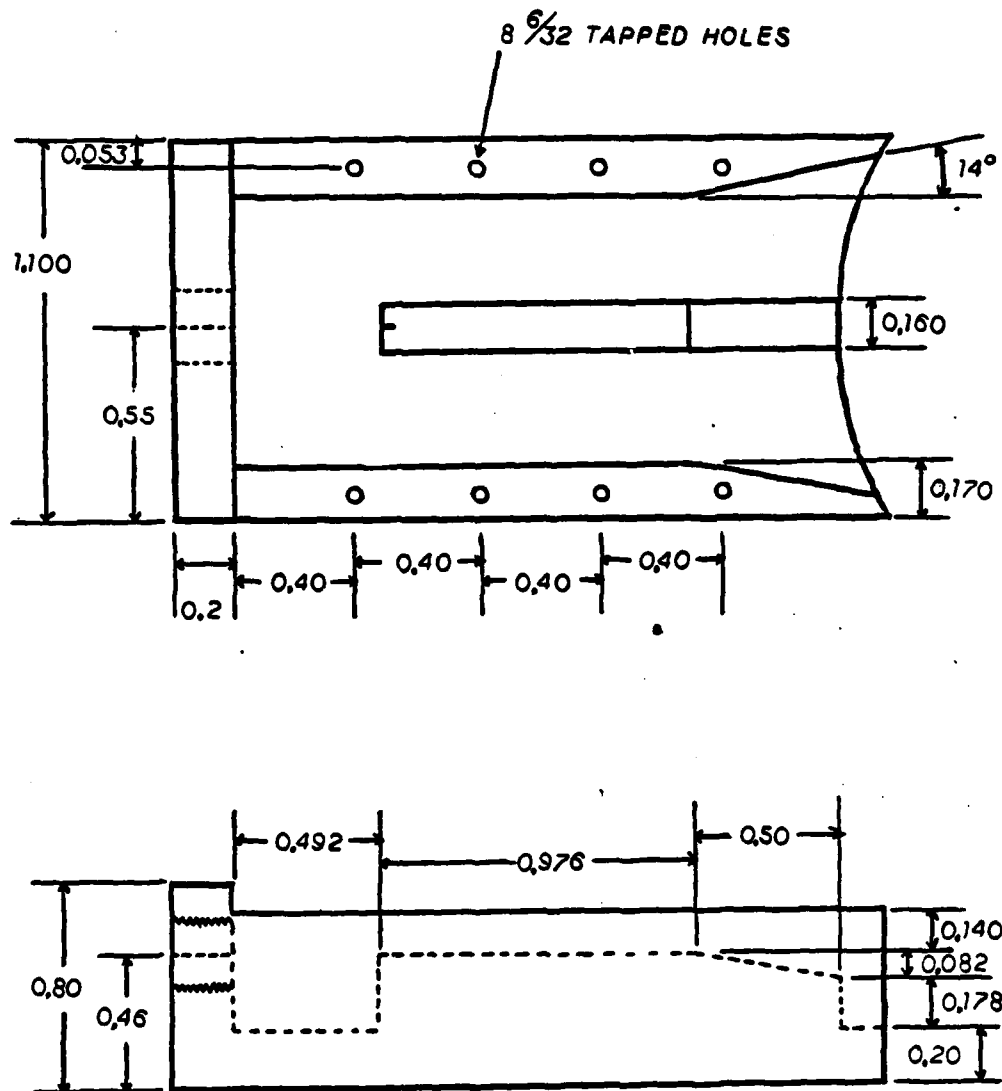


Figure A2.2 6 GHz Waveguide Launcher

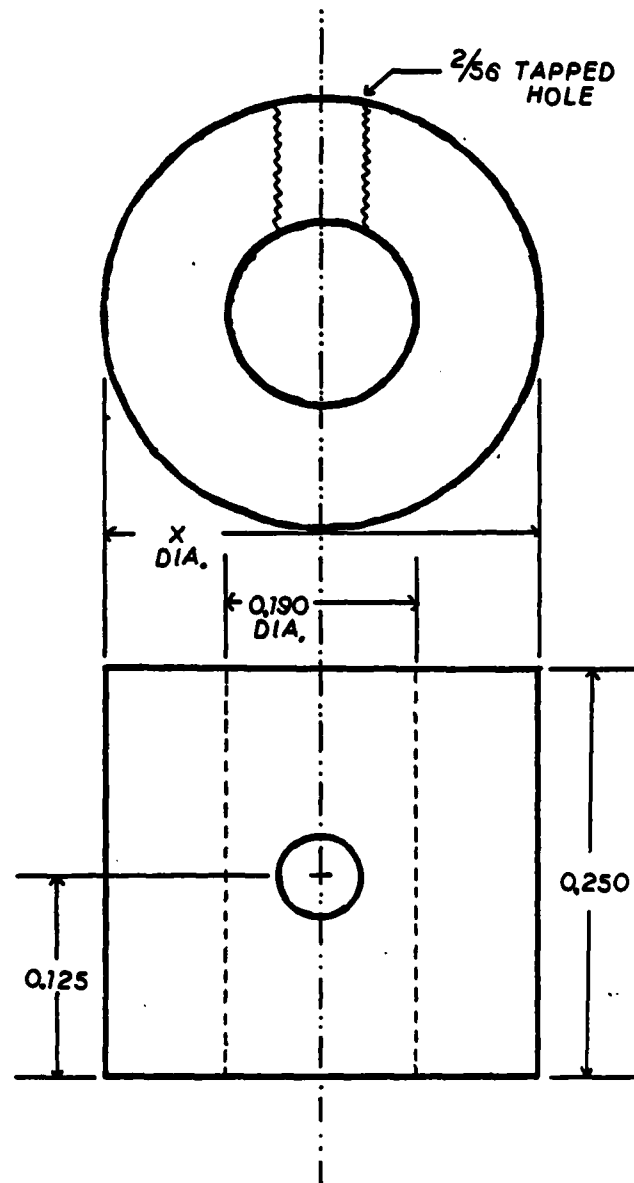


Figure A2.3 12 GHz quarter wavelength tuning stub,  $x=0.284$  inches for 25 ohms.

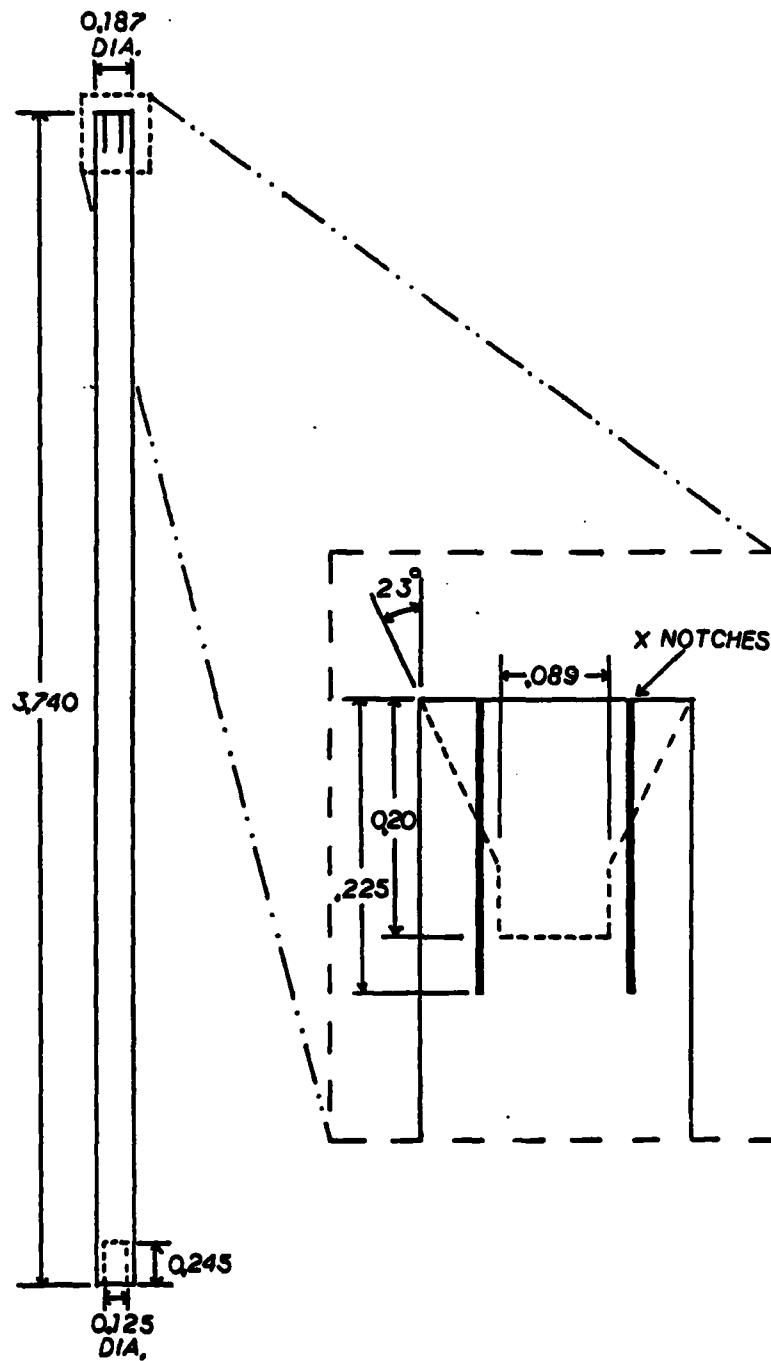


Figure A2.4 Sliding stub tuner center conductor

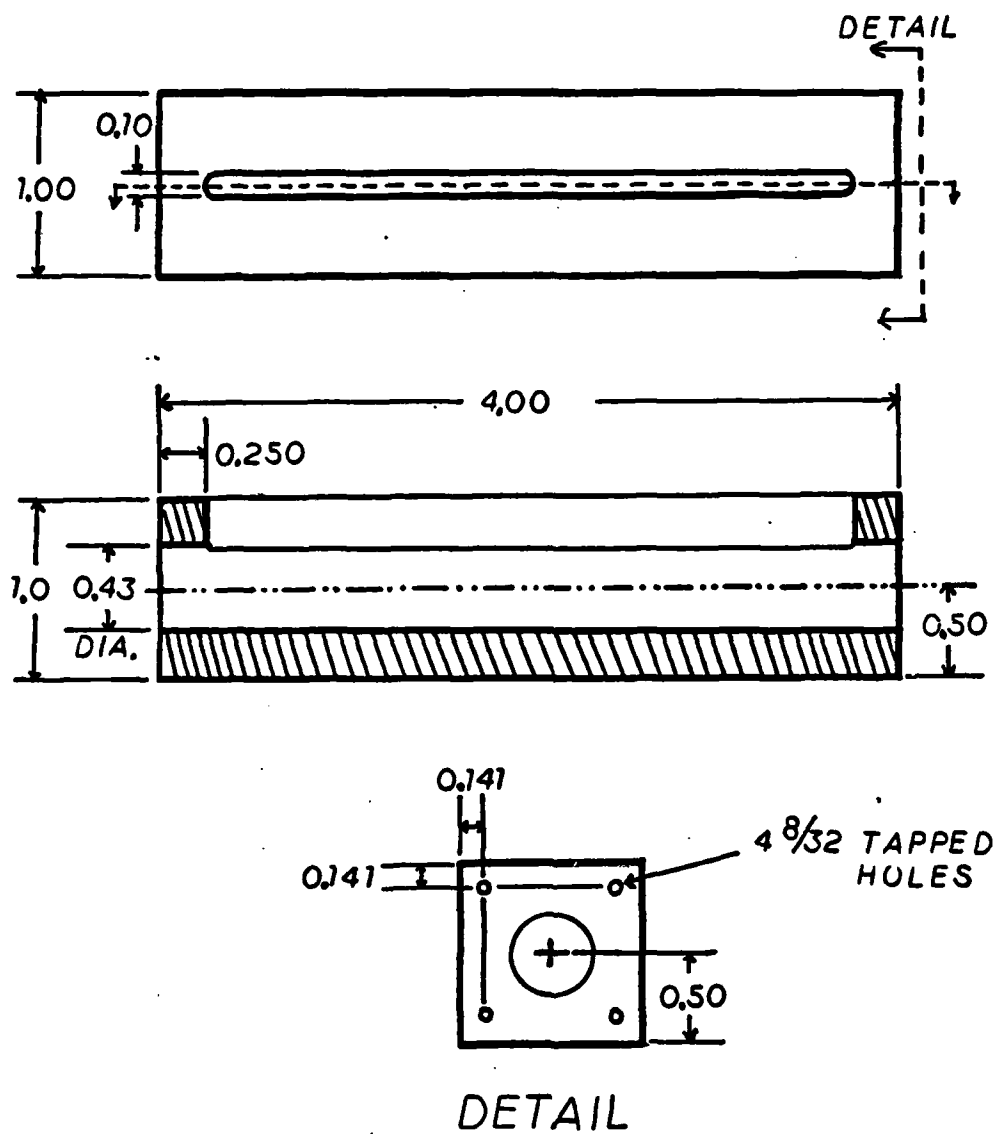


Figure A2.5 Sliding stub tuner body

APPENDIX 3  
Power Supply Circuits





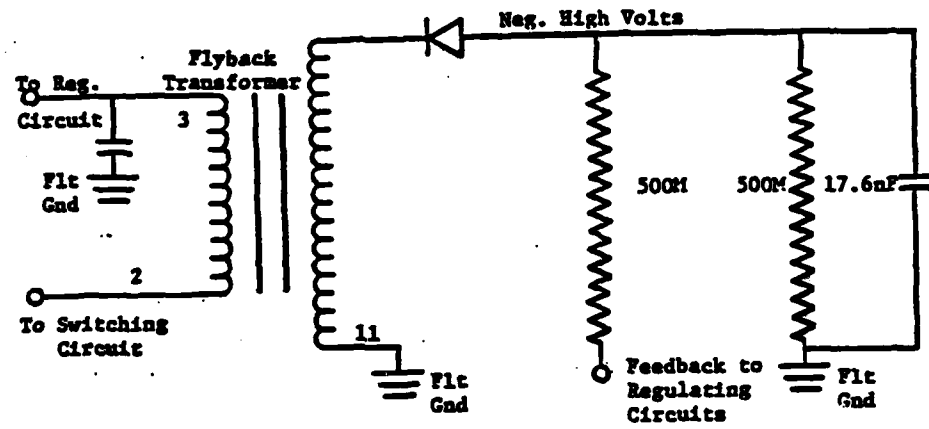


Figure A2.7 High voltage circuit

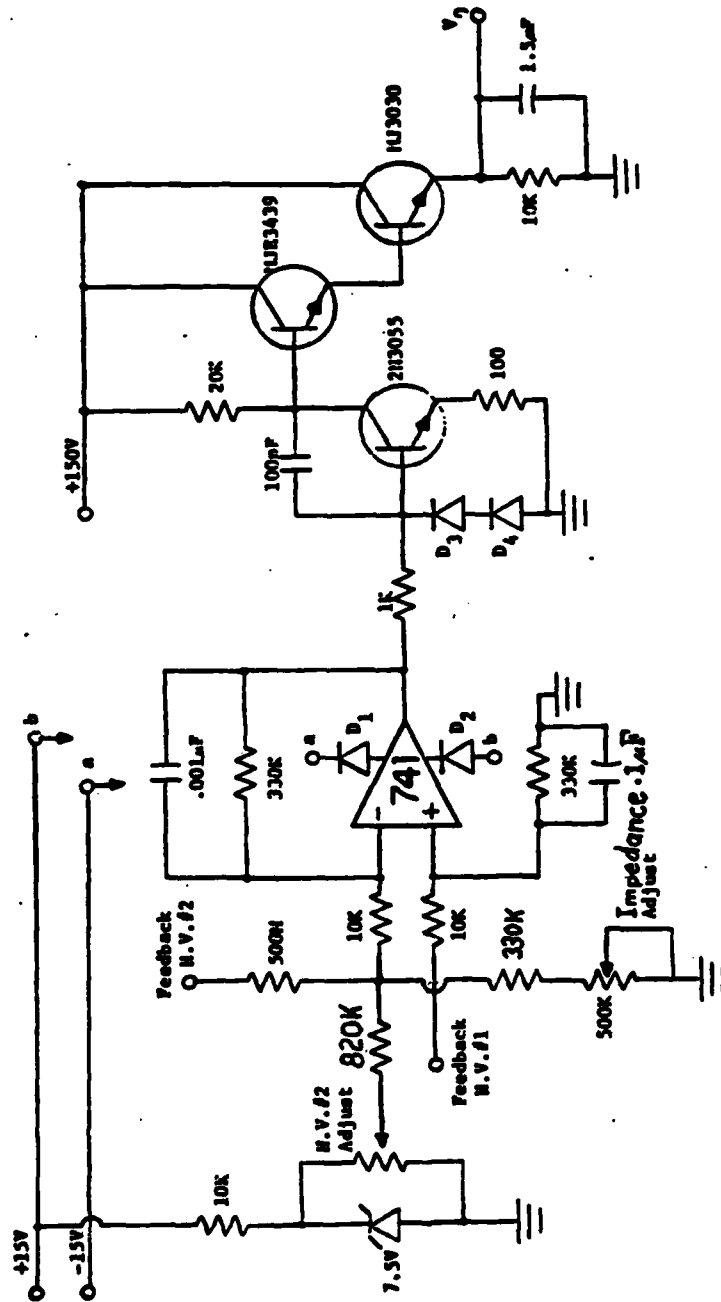


Figure A2.8 Regulating circuit H.V.#2

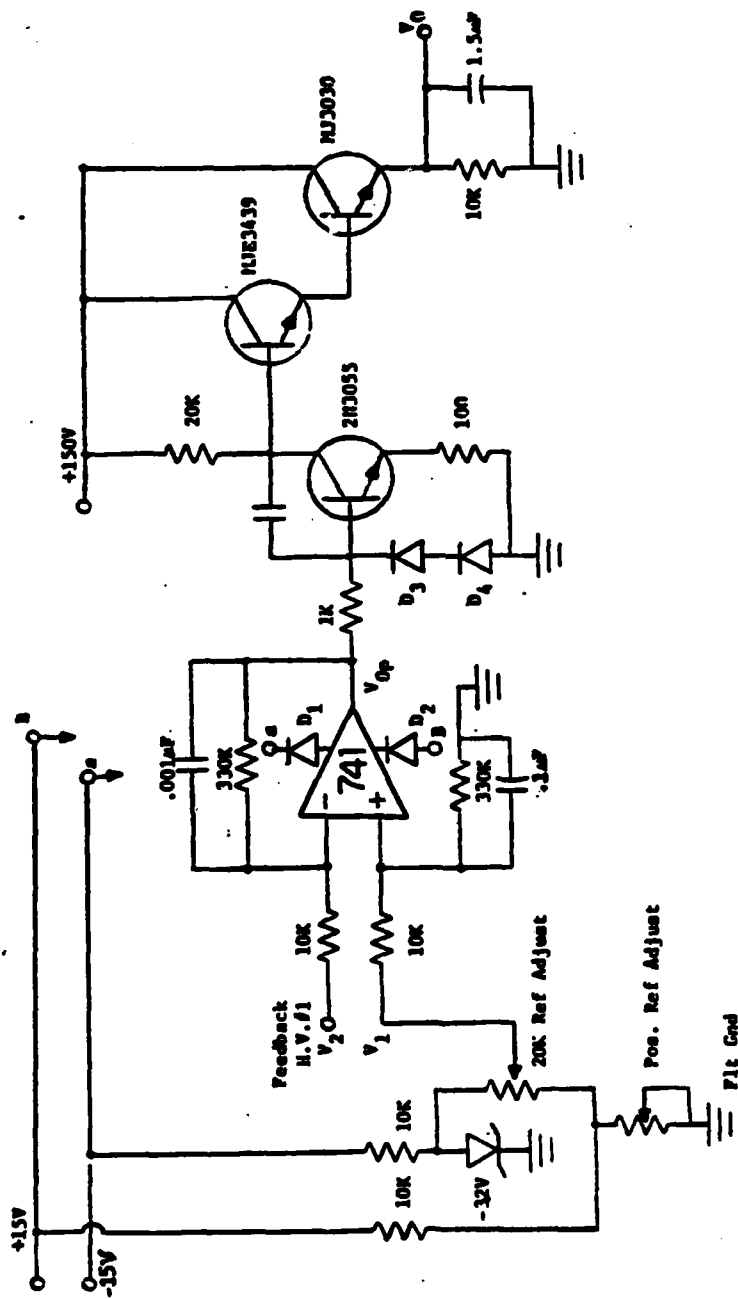
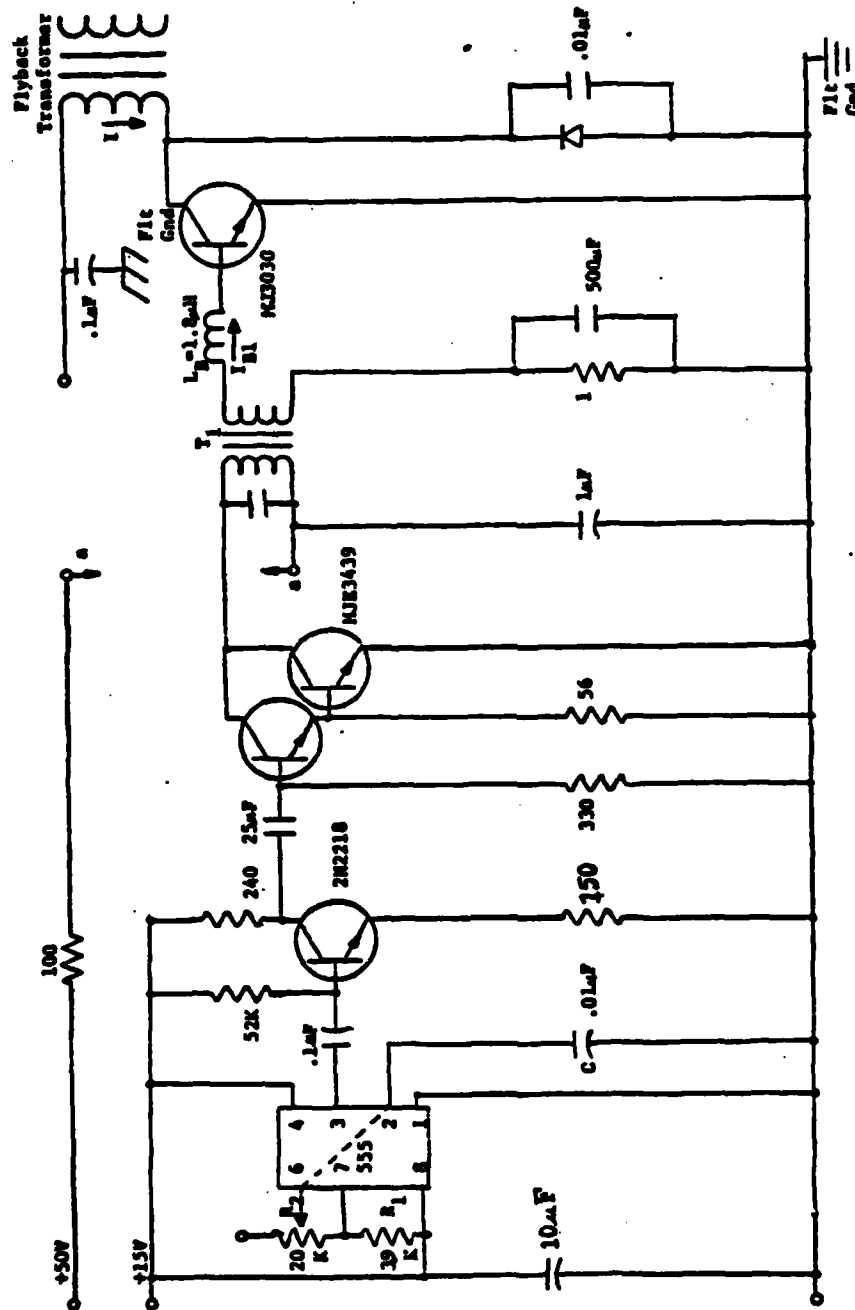


Figure A2.9 Regulating circuit H.V.#1



**Figure A2.10 Switching circuit**

APPENDIX 4

## Lumped Element Sample Model

At the node called the package post point in Figure 3.9, one can relate the three currents through equation A.4.1:  $I_1$  is the current through the ring capacitance into the node;  $I_2$  is the current through the parallel combination of the package capacitance and the load impedance; and  $I_A$  is the excitation current to be examined. So

$$I_1 = I_2 - I_A \quad (\text{A4.1})$$

and

$$Z' = \frac{Z_L}{1 + j\omega C_p Z_L} \quad (\text{A4.2})$$

By applying Kirchoff's voltage law to the external loop one finds

$$\frac{I_1}{j\omega C_r} + Z' \cdot I_2 + j\omega L_b I_2 = 0 \quad (\text{A4.3})$$

substituting (A4.1) for  $I_1$  yields

$$I_2 = \frac{\frac{I_A}{j\omega C_r}}{1 + j\omega C_r Z' - \omega^2 C_r L_b} \quad (\text{A4.4})$$

The measured signal is then just

$$V_m = Z' \cdot I_2 = \frac{Z_L I_A}{1 - \omega^2 C_r L_b + j\omega Z_L (C_p + C_r - \omega^2 C_p C_r L_b)} \quad (A4.5)$$

which can be described as

$$V_m = |Z_{eff}| \angle \phi_{eff} * I_A \quad (A4.6)$$

Equations A4.5 and A4.6 demonstrate the significance of the bond area capacitance phase contributions to the measured phase of the signal. As the applied reverse bias decreases below the punched-through value,  $C_p$  increases and changes the phase contribution of the effective impedance in A4.6. To minimize the effect of this capacitance shift the bond area can be reduced, increasing the shunt impedance across the actual current source. Measurements could also be performed with reverse applied bias voltages near or above the punched-through value. The variation of bond area capacitance should be very small in this case as the depletion depth does not change a great deal.

## 8. BIBLIOGRAPHY

1. J.B. Gunn, "Microwave Oscillations of Current III-V Semiconductors", Solid State Communications, 1:88, 1963.
2. J.G. Ruch and G.S. Kino, "Measurement of the Velocity-Field Characteristic of Gallium Arsenide", Applied Physics Letters, Vol. 10, January 15, 1967.
3. A.G.R. Evans and P.N. Robson, "Drift Mobility Measurements in Thin Epitaxial Semiconductor Layers Using Time-of-Flight Techniques", Solid State Electronics, Vol. 17, pp. 805-812, 1974.
4. T.H. Windhorn, T.J. Roth, L.M. Zinkiewicz, O.L. Gaddy and G.E. Stillman, "High Field Temperature Dependant Electron Drift Velocities in GaAs", Applied Physics Letters, Vol. 40, pp. 513-515, March 15, 1982.
5. T.H. Windhorn, L.W. Cook and G.E. Stillman, "The Electron Velocity-Field Characteristic for n-InGaAs at 300K", IEEE Electron Device Letters, Vol. EDL-3 No.1, January 1982.
6. P.M. Smith, M. Inoue and J. Frey, "Electron Velocity in Si and GaAs at Very High Electric Fields", Applied Physics Letters, Vol. 37, November 1, 1980.



7. J. Pozela and A. Reklaitis, "Electron Transport Properties in GaAs at High Electric Fields", Solid State Electronics, Vol. 23, pp. 927-933, 1980.
8. S.L. Von Rump, F.J. Rosenbaum, R.E. Goldwasser, M.H. Riess, G.M. Homsey and J.M. Bornholdt, "System for the Transport Analysis of Semiconductor Materials", Washington University in St. Louis, O.N.R. Report 80-2, October, 1980.
9. R.U. Martinelli, "Electron-beam Penetration in GaAs", Journal of Applied Physics, Vol. 44, July 1973.
10. M.L. Cohen and T.K. Bergstresser, "Band Structures and Pseudopotentials Form Factors for Fourteen Semiconductors of the Diamond and Zinc-blende Structures", Physical Review, Vol.141, January 1966.

DISTRIBUTION LIST  
CONTRACT N00014-79-C-0840

Code 414	4	Dr. C. Krumn	1
Office of Naval Research		Hughes Research Laboratory	
Arlington, VA 22217		3011 Malibu Canyon Road	
		Malibu, CA 90265	
Naval Research Laboratory			
4555 Overlook Avenue, S.W.		Mr. Lothar Wandinger	1
Washington, D.C. 20375		ECOM/AMSEL/TL/IJ	
Code 6811	1	Fort Monmouth, NJ 07003	
6850	1		
6820	1	Dr. William Lindley	1
6851	1	MIT	
		Lincoln Laboratory	
Defense Documentation Center	12	F124 A, P.O. Box 73	
Building 5, Cameron Station		Lexington, MA 02173	
Alexandria, VA 22314			
Dr. Y. S. Park	1	Commander	1
AFWAL/DHR		U.S. Army/ERADCOM	
Building 450		ATTN: V. Gelnovatch, DELET-M	
Wright-Patterson AFB		Fort Monmouth, NJ 07703	
Ohio 45433			
		RCA	1
Texas Instruments	1	Microwave Technology Center	
Central Research Lab		Dr. F. Sterzer	
M.S. 134		Princeton, NJ 08540	
13500 North Central Expressway			
Dallas, TX 75265		Commander	1
ATTN: Dr. W. Wisseman		Naval Electronics Systems Command	
		ATTN: J. P. Letellier, Code 6142	
Dr. R. M. Malbon/M.S. 1C	1	Washington, D.C. 20360	
Avantek, Inc.			
3175 Bowers Avenue		Commander	1
Santa Clara, CA 94304		Naval Air Systems Command	
		ATTN: A. Glista, Jr., AIR 34	
Dr. R. Bierig	1	Washington, D.C. 20361	
Raytheon Company			
28 Seyon Street		Dr. R. Bell, K-101	1
Waltham, MA 02154		Varian Associates, Inc.	
		611 Hansen Way	
Dr. Mike Driver	1	Palo Alto, CA 94304	
Westinghouse Research and			
Development Center			
Beulah Road			
Pittsburgh, PA 15235			
Dr. F. Eisen	1		
Rockwell International			
Science Center			
P.O. Box 1085			
Thousand Oaks, CA 91360			

Hewlett-Packard Corporation Dr. Robert Archer 1501 Page Road Palo Alto, CA 94306	1	Dr. Ken Weller MS/1414 TRW Systems One Space Park Redondo Beach, CA 90278	1
Watkins-Johnson Company E. J. Crescenzi, Jr./ K. Niclas 3333 Hillview Avenue Stanford Industrial Park Palo Alto, CA 94304	1	Professor L. Eastman Phillips Hall Cornell University Ithaca, NY 14853	1
Commandant Marine Corps Scientific Advisor (Code AX) Washington, D.C 20380	1	Professor Hauser and Littlejohn Department of Electrical Engr. North Carolina State University Raleigh, NC 27607	1
Communications Transistor Corp. Dr. W. Weisenberger 301 Industrial Way San Carlos, CA 94070	1	Professor J. Beyer Department of Electrical and Computer Engineering University of Wisconsin Madison, WI 53706	1
Microwave Associates Northwest Industrial Park Drs. F. A. Brand/J. Saloom Burlington, MA 01803	1	W. H. Perkins Electronics Lab 3-115/B4 General Electric Company P.O. Box 4840 Syracuse, NY 13221	1
Commander, AFAL AFWAL/AADM Dr. Don Rees Wright-Patterson AFB, OH 45433	1	Bryan Hill AFWAL/AAD E Wright-Patterson AFB, OH 45433	1
Professor Walter Ku Phillips Hall Cornell University Ithaca, NY 14853	1	H. Willing/Radar Directorate BMD - Advanced Technical Center P.O. Box 1500 Huntsville, AL 35807	1
Commander Harry Diamond Laboratories Mr. Horst W. A. Gerlach 800 Powder Mill Road Adelphia, MD 20783	1		
A.G.E.D. 201 Varick Street 9th Floor New York, NY 10014	1		